Cellular and Molecular Life Sciences (2022) 79:389
https://doi.org/10.1007/s00018-022-04417-9



ORIGINAL ARTICLE

# EWI2 prevents EGFR from clustering and endocytosis to reduce tumor cell movement and proliferation

**Chenying Fu[1] · Jie Wang[1] · Sandeep Pallikkuth[2] · Yingjun Ding[1] · Junxiong Chen[1] · Jonathan D. Wren[3] · Yuchao Yang[1] · Kwong-Kwok Wong[4] · Hiroyasu Kameyama[1] · Muralidharan Jayaraman[1] · Anupama Munshi[1] · Takemi Tanaka[1] · Keith A. Lidke[2] · Xin A. Zhang[1]**

Received: 18 February 2022 / Revised: 27 May 2022 / Accepted: 6 June 2022 / Published online: 30 June 2022


## Abstract

EWI2 is a transmembrane immunoglobulin superfamily (IgSF) protein that physically associates with tetraspanins and integrins. It inhibits cancer cells by influencing the interactions among membrane molecules including the tetraspanins and integrins. The present study revealed that, upon EWI2 silencing or ablation, the elevated movement and proliferation of cancer cells in vitro and increased cancer metastatic potential and malignancy in vivo are associated with (i) increases in clustering, endocytosis, and then activation of EGFR and (ii) enhancement of Erk MAP kinase signaling. These changes in signaling make cancer cells (i) undergo partial epithelial-to-mesenchymal (EMT) for more tumor progression and (ii) proliferate faster for better tumor formation. Inhibition of EGFR or Erk kinase can abrogate the cancer cell phenotypes resulting from EWI2 removal. Thus, to inhibit cancer cells, EWI2 prevents EGFR from clustering and endocytosis to restrain its activation and signaling.

**Keywords** Clathrin-mediated endocytosis · Epithelial-to-mesenchymal transition · MAPK signaling · Membrane spatial heterogeneity · And integrin

## Abbreviations

| | |
|---|---|
| Ab | Antibody |
| BSA | Bovine serum albumin |
| CAMs | Cell adhesion molecules |
| CHC | Clathrin heavy chain |
| ECM | Extracellular matrix |
| EGFR | Epidermal growth factor receptor |
| EMT | Epithelial-to-mesenchymal transition |
| FBS | Fetal bovine serum |
| FN | Fibronectin |
| HB-EGF | Heparin-binding EGF-like growth factor |
| IgSF | Immunoglobulin superfamily |
| KO | Knockout |
| KD | Knockdown |
| LN | Laminin |
| mAb | Monoclonal antibody |
| MAPK | Mitogen-activated protein kinase |
| pAb | Polyclonal antibody |
| PBS | Phosphate buffered saline |
| PFA | Paraformaldehyde |
| PRAD | Prostate adenocarcinoma |
| ROI | Region of interest |
| STORM | Stochastic optical reconstruction microscopy |
| SR | Super-resolution |
| TEMD | Tetraspanin-enriched membrane domain |
| TUNEL | Terminal deoxynucleotidyl transferase dUTP nick end labeling |

Chenying Fu and Jie Wang have made equal contributions to this study.

✉ Xin A. Zhang
xin-zhang-1@ouhsc.edu

[1] University of Oklahoma Health Sciences Center, Oklahoma City, USA

[2] University of New Mexico, Albuquerque, USA

[3] Oklahoma Medical Research Foundation, Oklahoma City, USA

[4] University of Texas MD Anderson Cancer Center, Houston, USA

## Introduction

EWI2 or EWI2/PGRL or CD316 is a binding partner of tetraspanins [1–3], which physically associate with each other and with other membrane proteins such as integrins, IgSF proteins, proteases, and growth factors receptors. As all of these membrane proteins regulate cancer cell functions [2, 4–7], their associations could also be functionally impactful. EWI2 connections to various cancers are largely limited to its inhibitory roles in cancer invasiveness and metastasis, but whether EWI2 affects cancer formation and growth remains under-investigated.

It is well established that EGFR and its downstream Erk MAPK signaling drive cancer cell proliferation and movement [8]. EGFR and its ligand HB-EGF can be found in the multi-molecular complexes of tetraspanins, which also modulate EGFR signaling [9, 10]. For instance, tetraspanin CD9 complexes with EGFR and integrins and downregulates EGFR signaling by promoting EGFR endocytosis [11–13].

Tumor cells that underwent epithelial-to-mesenchymal transition (EMT) exhibit spindle/fibroblast-like morphology and enhanced motility [14, 15]. Tumor cells in different environments can also possess these properties or epithelial-mesenchymal plasticity [16]. Tumor cells with non-epithelial origin such as glioma and fibrosarcoma cells [15] inherit mesenchymal movement, while carcinoma cells [17] such as PC3 prostate cancer cells display more mesenchymal behaviors after EMT [18–21].

Here, we demonstrated that EWI2 regulates spatial dynamics of EGFR signaling, to inhibit locomotive behaviors and growth potential of cancer cells. EWI2 silencing or ablation promotes motogenic and mitogenic behaviors of prostate cells. Increased EGFR phosphorylation and Erk1/2 MAP kinase signaling upon EWI2 removal result from the increases in (i) molecular clustering of EGFR at the cell surface and (ii) endocytosis of EGFR. Thus, as a regulator for the membrane distribution and vesicular trafficking of EGFR, EWI2 inhibits cancer cell movement and proliferation in vitro and cancer formation and malignancy in vivo by limiting EGFR-Erk signaling and may become a therapeutic target against cancer.

## Materials and methods

### Antibodies and reagents

See all Abs used in this study in Table S1–2 and reagents in Table S3.

### Knockdown (KD) and knockout (KO) of EWI2

PC3 cells and Du145 cells, two types of human prostate cancer cell lines, were obtained from ATCC and cultured in complete DMEM media (DMEM containing 10% fetal bovine serum [FBS] and 1% penicillin/streptomycin).

The siRNA oligo against the target sequence GUU CUCCUAUGCUGUCUU of EWI2 mRNA was used to silence EWI2 expression [22]. PC3 cells or Du145 cells were transfected with the siRNA using Lipofectamine RNAiMAX. The experiments were performed 2 days post-transfection.

PC3-EWI2 KO cells were generated with CRISPR/Cas9 technology. Specifically, pX458 (SpCasp-2A-GFP) vector (Addgene, Watertown, MA) was digested with BbsI enzyme at 37 °C for 30 min and ligated with annealed oligonucleotides (Table S4) corresponding to small guide RNAs (sgRNAs) targeting exon 2 of the EWI2 gene (5′ GCGGGCAATCTTGAGCACCA 3′), for the generation of PX458-EWI2 KO construct. PC3 cells were seeded at a density of $0.5–1 \times 10^5$ cells/well in six-well plates and transfected with PX458-EWI2-KO construct (2.5 μg/well) by Lipofectamine3000. Cells were selected based on GFP expression by flow cytometry after 48–72 h. The collected cells were then amplified in culture for several days, followed by a second sort to select both EWI2- and GFP-negative cells. The collected cells were amplified in cell culture for several days and then further sorted with flow cytometry, to obtain the cells negative in both GFP and EWI2 expression. The pool of those sorted cell was used as PC3-EWI2 KO transfectant.

### Cell proliferation and survival assays

For anchorage-dependent cell proliferation, cells at different densities (2500, 5000, and 10,000 cells) in 100-μl culture media were seeded in 96-well plates. Cell proliferation was monitored by analyzing the occupied area of cell images over time in the Incucyte Live Cell Imaging System (Essen BioScience, Arbor, MI) and represented as fold change of increased confluence.

Cell survival was assessed with CCK8 assay by following the protocol of the manufacturer. After 24-h culture of equal number of cells ($5 \times 10^3$ cells/well of 96-well plate) from each group, the cells were replenished in fresh complete media and incubated with 10 μl of CCK-8 reagent at 37 °C for 4 h. The absorbance at 450 nm was measured with Perkin Elmer EnVision® Multilabel Reader (Perkin Elmer, Waltham, MA). Cell apoptosis was induced by TNF-α (20 nM) for 48 h and measured by cleaved Caspase 3 expression and TUNEL assay.

For anchorage-independent cell proliferation, a mixture of 0.75 ml of 2 × DMEM complete medium and 0.75 ml of 1% noble agar in deionized water were loaded into individual well of six-well plates. After the agar became solidified, each well was overlaid with the mixture containing 0.75 ml 2 × DMEM complete medium, 0.75 ml 0.6% noble agar in deionized water, $5 \times 10^3$ cells, and 1.3 µl DMSO with or without 15 nmol Gefitinib. After having been cultured for 4 weeks, colonies were fixed and stained with 0.1% crystal violet in 70% ethanol. The number and size of colonies were examined microscopically.

## Cell movement assays

Directional solitary cell migration was examined with a Transwell migration assay. Transwell inserts (Corning, Corning, NY) were coated with fibronectin (FN), laminin (LN) 111 or laminin 411, and were then put in completed medium. Cells were suspended in FBS-free DMEM medium, loaded into inserts, and incubated at 37 °C for 3–6 h.

Random solitary cell migration was analyzed by live imaging with the Operetta High Content Imaging System (Perkin Elmer, Waltham, MA) for KD transfectants. The cells transfected with control or EWI2 siRNA were photographed once every 15 min for 16 h, starting from 48 h post-transfection. Gefitinib (10µM) was added in the medium for 32 h when rescue experiments were performed. The distance and speed of individual cell movements were analyzed with Columbus 2.3 software (Perkin Elmer, Waltham, MA). For KO transfectants, random migration was measured in the Transwell system. Briefly, inserts membranes were put in complete medium without coating extracellular matrix. $1 \times 10^5$ cells in 100 µl complete medium were added in the upper chamber. Migrated cells were fixed by 4% PFA and stained with 0.1% crystal violet after 6 h. Cells were counted under an inverted microscope (Olympus, Bartlett, TN).

Collective cell migration was evaluated in a wound-healing assay. For knock down system, PC3 cells were cultured in six-well plates and were then knocked down with EWI2 siRNA. After the cells reached confluence, wounds were created with pipette tips by scratching the monolayer. During 16–24 h of healing, wound closure was analyzed using an inverted light microscope every 4 h. Wound closure was imaged and analyzed with Image J software. For KO system, $1.5 \times 10^5$ cells were added in each well of a 96-well plate to form a confluent monolayer. The gap was made by the woundmaker tool (Essen BioScience, Arbor, MI). Then, the detached cells were removed gently. 100 µl FBS-free culture medium was added to each well. Relative wound density (cell density in the wound area / cell density outside of the wound area) was measured in the Incucyte LiveCell Imaging System (Essen BioScience, Arbor, MI).

Cell invasion was examined with Transwell inserts that were coated with Matrigel. The cells were added on the gel and incubated overnight at 37 °C, 5% $CO_2$. The cells were pre-treated with Gefitinib (10 µM) for 32 h or Ravoxertinib (1 µM) for 16 h prior to the experiments when rescue experiments were performed. The cells that invaded through the inserts were fixed with 4% PFA, stained with Diff-Quick solution or 0.1% crystal violet and then imaged. Cell number was counted using Image J software.

## Cell–matrix adhesion assays

Cell–matrix adhesion was examined on FN- or LN111-coated plates. After 1 h of incubation, cells were rinsed with serum-free DMEM three times to remove non-adherent cells. The adherent cells were stained with Diff-Quick solution, imaged, and quantified with Image J software.

## Flow cytometry and imaging flow cytometry

Cells were incubated with primary Abs on ice, followed by washes with cold PBS and subsequent staining with fluorochrome-conjugated secondary Abs on ice. After staining, the cells were examined with an automated FourColor Benchtop flow cytometer (BD Biosciences, San Diego, CA) or Amnis ImageStreamX Mk II Imaging flow cytometer (Luminex, Austin, TX). The traditional and imaging flow cytometry data were analyzed with the Flowjo7.6.1 program (BD Biosciences, San Diego, CA) and IDEAS program (Amnis part of EMD Millipore, Seattle, WA), respectively.

## Western blot

Cells were lysed with RIPA buffer on ice for 30 min. After centrifugation at 13,000×*g* for 15 min, soluble portions of the cell lysates were separated by SDS-PAGE and then electrically transferred to nitrocellulose membranes. The membranes were blocked with fat-free milk and then blotted sequentially with primary Abs and horseradish peroxidase-conjugated secondary Abs, followed by chemiluminescence.

## Fluorescence microscopy

Cells were fixed with 3% PFA, and permeabilized with 0.1% Brij98 in PBS for 90 s or 0.1% Triton X-100 in PBS for 5 min. Then, the cells were incubated sequentially with primary Abs and fluorochrome-conjugated secondary Abs. Cells were then examined and imaged with Leica SP2 or SP8 confocal microscope equipped with a 63×Plan APO 1.4 NA oil immersion objective (Leica Microsystems, Buffalo Grove, IL). ImageJ software was used for image analysis.

When epithelial-to-mesenchymal transition was analyzed, PC3 cells were seeded on Matrigel and stained with

Alexa Fluor 488-conjugated phalloidin. Gefitinib (30 nM) or Ravoxertinib (1 μM) was applied to treat cells overnight before seeding cells.

### Immunohistochemistry

Slides were de-paraffinized and rehydrated. Sodium citrate (10 mM, pH 6.0) was used to perform antigen retrieval. Slides were blocked by 1% BSA in PBS, incubated with primary antibody and secondary antibody and treated with DAB reagents. Random sections were cut from each tumor tissues (see below), and randomly selected fields were examined in each section. The average value from each section was used as one readout.

### Endocytosis assay

Cells cultured on glass coverslips were chilled on ice for 10 min, then washed with cold live cell imaging solution (HEPES-based buffer at pH 7.4, 20 mM glucose, and 1% BSA), and incubated with 2 μg/ml of pHrodo green EGF conjugate in the solution at 37 °C for 15 min, followed by washes with the solution and fixation with 3% PFA. The cells were then imaged under a LeicaSP2 or SP8 confocal microscope with excitation wavelength of 509 nm, emission 518 nm, and a 63 × Plan APO 1.4 NA oil immersion objective (Leica Microsystems, Buffalo Grove, IL). The images were analyzed for internalized EGF and its colocalization with clathrin heavy chain (CHC) or caveolin-1 by ImageJ software.

EGFR mAb GFR450, which is against extracellular domain of human EGFR, was used as another probe to examine EGFR endocytosis. PC3 cells were incubated with the mAb (20 μg/ml) at 37 °C for 15 min. The following procedures were the same as described above.

### Super-resolution (SR) imaging and data analysis

Cells were cultured in the eight-well chambered coverglass (ThermoFisher, Rockford, IL) for 12 ~ 24 h, treated with human EGF (25 nM in PBS) for 3 min, and washed once with PBS. The cells were then fixed with 3% glyoxal solution at room temperature for 1 h and washed sequentially with 0.1% $NaBH_4$ in PBS for 5 min and 10 mM Tris in PBS for 5 min twice at room temperature, followed by block with 5% BSA, 0.05% Triton X-100 in PBS for 15 min. The cells were labeled with 4 μg/ml of AlexaFluor 647-conjugated EGFR antibody in 2% BSA, 0.05% Triton X-100 in PBS at room temperature for 1 h, washed with 2% BSA, 0.05% Triton X-100 in PBS at room temperature for 5 min thrice and with PBS for 5 min once.

The coverslip with fixed and labeled cells was mounted on an Attofluor cell chamber (ThermoFisher, Rockford, IL) with 1.5 ml of the imaging buffer, which consisted of an enzymatic oxygen-scavenging system and primary thiol: 50 mM Tris, 10 mM NaCl, 10% glucose, 168.8 U/ml glucose oxidase, 1,404 U/ml catalase, and 20 mM 2-Aminoethanethiol, pH 8. The chamber was sealed by placing an additional coverslip over the chamber, and the oxygen-scavenging reaction was allowed to proceed for 15 min at room temperature before the imaging started. Imaging was performed using a custom-built microscope controlled by custom-written software in MATLAB (MathWorks, Natick, MA). A sCMOS camera (C11440-22CU; Hamamatsu Photonics, Bridgewater, NJ) was used to collect SR data. A 647-nm laser (500 mW 2RU-VFL-P; MPB Communications Inc., Pointe-Claire, Quebec) was used as the excitation laser. The objective had an NA of 1.49 (APON 60 × OTIRF; Olympus, Bartlett, TN), and the filters consisted of a 708/75-nm filter (FF01-708/75-25; Semrock, Rochester, NY) for SR image emission path, and a 640/8-nm laser diode cleanup filter (LD01-640/8–12.5; Semrock, Rochester, NY). A total of 40,000 images (20 datasets of 2000 frames at 100 Hz) were recorded and stored during data acquisition on each cell. Correction for sample drift was performed before each dataset using brightfield-registration. Data were collected for at least 12 different cells from each coverslip.

The data were analyzed via a 2D localization algorithm based on maximum likelihood estimation [23]. The localized emitters were filtered through thresholds of a maximum background photon counts at 200, a minimum photon counts per frame per emitter at 250, and a data-model hypothesis test with a cutoff $p$ value at 0.01 [24]. The accepted emitters were used to reconstruct the super-resolution image. Each emitter was represented by a 2D-Gaussian with $\sigma_x$ and $\sigma_y$ equal to the localization precisions, which were calculated from the Cramér-Rao Lower Bound.

Clustering analysis of dSTORM data was performed using the density-based DBSCAN algorithm implemented in MATLAB as part of a package of local clustering tools (https://stmc.unm.edu/) [25, 26]. Parameters chosen were (i) a maximal distance between neighboring cluster points of $\varepsilon = 40$ nm and (ii) a minimal cluster size of three observations. Cluster boundaries were produced with the MATLAB "boundary" function using a default methodology that produced contours halfway between a convex hull and a maximally compact surface enclosing the points. The cluster areas within these boundaries were then converted into the radii of circles of equivalent area for a more intuitive interpretation. 10–15 ROIs of size 5 μm × 5 μm (10 $\mu m^2$) were selected within each super-resolution cell image from which statistics for the equivalent radii were collected per ROI. A $p$ value was also calculated for comparing distributions via the two-sample Kolmogorov–Smirnov goodness-of-fit hypothesis test. A $p$ value near 1 suggests the two distributions which are being sampled are drawn from the same

underlying continuous population, while a *p* value near zero suggests the underlying distributions are different.

### Extracellular matrix (ECM) deposition

PC3 cells were seeded on the coverslips and removed by 1% Triton X-100 in PBS after 48 h. ECM was fixed by 4% PFA, incubated with fibronectin antibody or collagen IV antibody, and sequent secondary antibodies. Images were taken under SP8 confocal microscope (Leica Microsystems, Buffalo Grove, IL) and analyzed by ImageJ software. Cell numbers were quantified by optical density (OD) values after crystal violet staining. Tissue sections from the tumor tissues (see below) were stained with Sirius Red.

### Tumorsphere formation assay

PC3 cells were suspended in the tumorsphere-formation media (DMEM supplemented with 20 ng/ml EGF, 10 ng/ml FGF, 5 µg/ml insulin, 0.4% BSA, and 1 × B27) at the concentration of 1 cell per µl of the medium. Two hundred cells were added into each well of a 96-well ultra-low attachment plate (Corning, Corning, NY). After 10-day incubation, tumorsphere numbers in each well were counted under a microscope. Tumorsphere formation efficiency was calculated as a percentage of the number of tumorspheres formed from the number of cells seeded initially [27, 28].

### Tumor initiation and growth in vivo

One million PC3 cells in 100 µl PBS were injected subcutaneously into 8-week-old male NU/J nude mice (Foxn1$^{nu}$). For those mice with treatment, Gefitinib (500 mg/kg) was administrated by gavage at 1-, 2-, 3-, 5-, and 7-week post-injection. Mouse body weights and tumor sizes were measured every 4 days. The volume was calculated as length × width$^2$ × 0.52. Tumor tissues were collected 8 weeks after injection. The final tumor weight was measured.

### Experimental metastasis

PC3 transfectant cells (one million cells in 100 µl PBS per mouse) were injected through tail veins into 8-week-old male NU/J nude mice (Foxn1$^{nu}$). Lung tissues were collected 4 weeks after the injection. Metastatic lesions were examined in randomly selected tissue sections. Ravoxertinib (30 mg/kg/day) was administrated post-injection by gavage on a daily basis for 21 days.

### Bioinformatics analyses

Comparison of EWI2 mRNA levels between prostate adenocarcinoma (PRAD) and normal prostate tissues based on The Cancer Genome Atlas (TCGA) was obtained from MEXPRESS (https://mexpress.be/) and UALCAN (http://ualcan.path.uab.edu/analysis.html). EWI2 alteration in different types of cancers was generated from cBioPortal (https://www.cbioportal.org/). Dataset was selected as TCGA Pan-Cancer Atlas. Kaplan–Meier survival curves for EWI2 in TCGA data were plotted using GEPIA (http://gepia.cancer-pku.cn/). Patients were divided by median EWI2 expression levels. Correlations of EWI2 with EGFR, HER2, and HER3, and with MEK1, MEK2, Erk1, and Erk2 in gene expression in PRAD were examined in GEPIA.

### Statistical analyses

The incidence of tumor formation was compared using Chi-square test. All other data, based on at least three individual experiments, were compared using two-tailed Student's *t* test. Kaplan–Meier survival curve was plotted and analyzed with Log-rank (Mantel-Cox) test. Analyses were conducted with SPSS 13.0 or GraphPad 7 software. $p < 0.05$ was considered statistically significant for all statistical analyses.

## Results

### EWI2 inhibits tumor cell movement of certain modalities.

PC3 cells express an intermediate level of EWI2 (Figure S1), compared to other cells [3]. To determine the cellular functions of EWI2, we silenced EWI2 in PC3 cells using siRNA (Figure S1A and S1B) and ablated EWI2 using CRISPR-Cas9 (Figure S1C and S1D).

Since EWI2 overexpression inhibits cell movement, [3, 29] we examined the impact of EWI2 removal on cell movement. Directional solitary cell migration onto fibronectin (FN), laminin-111 (LN111), and laminin-411 (LN411) were markedly enhanced upon EWI2 KD and KO (Fig. 1A, S2A, and S2B). The invasiveness through Matrigel was also significantly increased upon EWI2 silencing (Fig. 1B, F, S2A, and S2B). Using Operetta system, we also examined random solitary cell migration on 3D collagen-I gel and found that the speed and distance of random migration were elevated on collagen-I gel upon EWI2 KD or KO (Fig. 1C, G). EWI2 KD or KO did not alter the ability of PC3 cells to heal wounds, a type of collective cell migration (Fig. 1D). Taken together, these findings indicate that EWI2 inhibits (i) cell invasion through Matrigel, (ii) directional solitary cell migration onto various ECMs, and (iii) random or non-directional migration but does not affect collective cell migration as measured by wound healing.

In accordance with the changes in cell movement in vitro, staining of vimentin, an EMT indicator, was increased in the

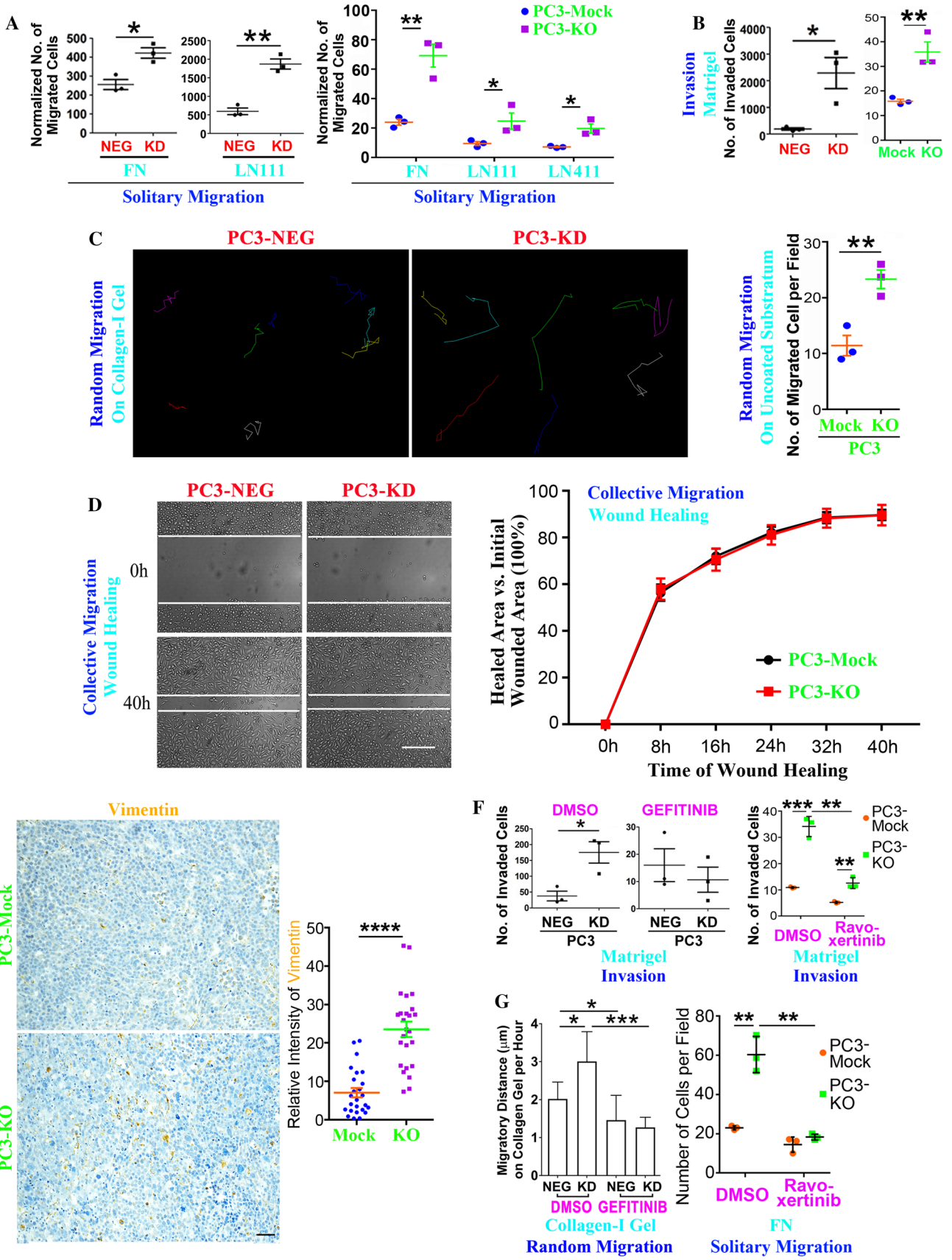
A
Normalized No. of Migrated Cells
NEG KD
FN
LN111
Solitary Migration
PC3-Mock
PC3-KO
LN411
B
Invasion
Matrigel
No. of Invaded Cells
Mock KO
C
PC3-NEG
PC3-KD
Random Migration
On Collagen-I Gel
On Uncoated Substratum
No. of Migrated Cell per Field
PC3
D
Collective Migration
Wound Healing
0h
40h
Healed Area vs. Initial Wounded Area (100%)
Time of Wound Healing
E
Vimentin
PC3-Mock
PC3-KO
Relative Intensity of Vimentin
F
DMSO
GEFITINIB
Ravo-xertinib
G
Migratory Distance (μm) on Collagen Gel per Hour
Number of Cells per Field
Collagen-I Gel
Random Migration
FN

◂**Fig. 1** EWI2 removal promotes the migration and invasion of tumor cells. **A** EWI2 in PC3 cells was either silenced with siRNA or ablated with CRISPR-Cas9 (see Figure S1 for details) and analyzed in Trans-well migration assay. Migration of the cells was examined with Transwell inserts coated with FN (10 µg/ml), LN111 (10 µg/ml), or LN411 (10 µg/ml). Numbers of the KD (left panel) and KO (right panel) cells that migrated through the inserts were counted and compared between groups statistically (mean ± SD, $n=3$ independent experiments). *$p<0.05$, **$p<0.01$. **B** PC3 cells transfected with control siRNA (NEG) or EWI2 siRNA (KD) (left) or PC3-Mock and PC3-KO (right) were analyzed in invasion assay with Transwell inserts coated with Matrigel. Numbers of the cells that invaded through the Matrigel were counted and compared statistically (mean ± SD, $n=3$ independent experiments). *$p<0.05$, **$p<0.01$. **C** PC3 NEG and EWI2-KD cells were cultured on collagen gel for 24 h and then live-recorded by the Operetta high-content imaging system for cell movement for 16 h. The trajectories of individual migratory cells and the distances of cell movement on the gels per hour were analyzed with ImageJ software. The distances of cell movement are presented in panel **G**. (left) PC3-mock and PC3-EWI2-KO cells in complete medium on the upper side migrated to the lower chamber which was also filled with complete medium through non-coated membrane when random migration was investigated. Cell numbers were determined at 6 h after seeding cells. Number of migrated cells was compared by t-test and represented as mean ± SD ($n=3$ individual experiments). **$p<0.01$. (right) **D** Wound healing analysis. Light microscopic images were taken at 40 h after the wounds in PC3-NEG and -KD cell monolayers were created (left). Scale bar: 250 µm. Healing process for PC3-Mock and -KO cell monolayers were dynamically traced for 40 h (right). **E** Tumors formed PC3-Mock and -KO cells (see below) were sectioned, stained for vimentin in immunohistochemistry, and photographed by light microscopy. Intensities were quantified and presented mean ± SE ($n=5$ tumors/mice per group and five fields per tumor/mouse). ****$p<0.0001$. Scale bar: 75 µm. **F** Effects of EGFR inhibitor Gefitinib and Erk inhibitor Ravoxertinib on the invasiveness through Matrigel. The cells were pre-treated with DMSO or Gefitinib (10µM) for 32 h or Ravoxertinib (1 µM) for 16 h prior to the experiments. Numbers of cells that invaded through the Matrigel were counted and presented as mean ± SD (n = 3 independent experiments). *$p<0.05$, **$p<0.01$, and ***$p<0.001$. **G** Effects of EGFR inhibitor gefitinib and Erk inhibitor Ravoxertinib on the migration of PC3-NEG and -KD cells on collagen-I gel or FN. The experiments and analysis were performed as described in panel **C**. The cells were treated with DMSO or Gefitinib (10µM) for 32 h or Ravoxertinib (1 µM) for 16 h prior to and during the experiments. Cell migration on collagen-I gel was live-recorded by the Operetta High-content Imaging System for 16 h, while cell migration onto FN was assayed with Transwell insert as described above. The distances of cell migration on collagen-I gels per hour were quantified with ImageJ software (mean ± SE, $n=3$ independent experiments, and a dozen of cells were analyzed in each experiment), while the numbers of cells migrated onto FN through Transwell inserts were fixed, stained, and counted as described above (mean ± SD, $n=3$ independent experiments). *$p<0.05$, **$p<0.01$, and ***$p<0.001$. **H**. Lung metastasis was examined 4 weeks after tail vein injection. Five random sections were made for each mouse and 3–5 random fields were observed in each section. Incidence of lung metastasis was compared by Chi-square test. Average number of metastases per field of each mouse was analyzed by *t* test (mean ± SD, three mice in Mock group, nine mice in KO group). *$p<0.05$, and ***$p<0.001$. Scale bar: 700 µm

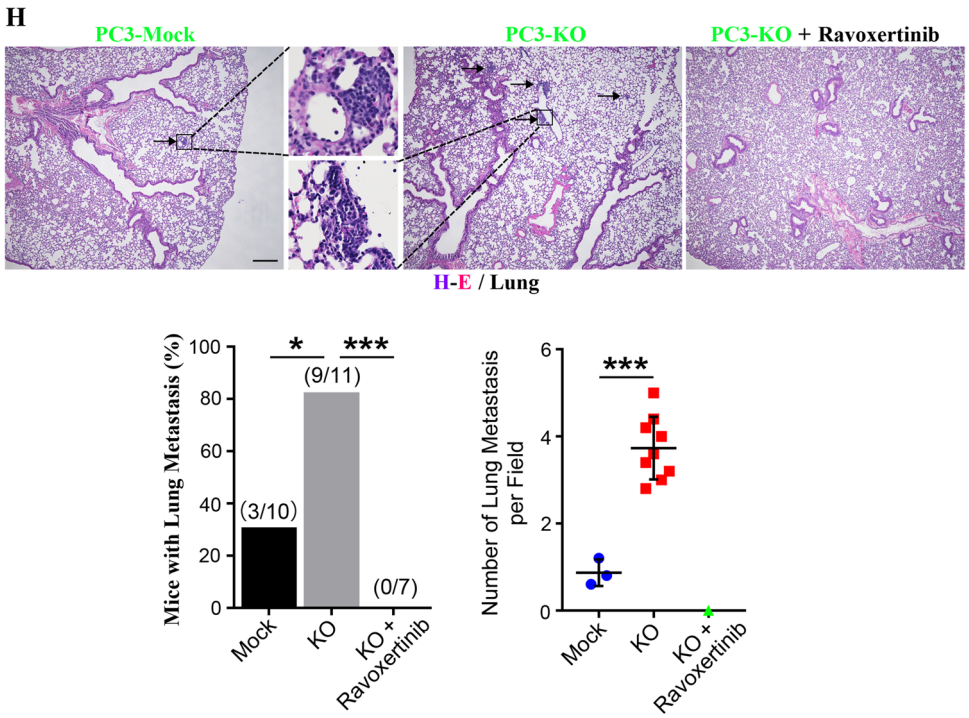


**Fig. 1** (continued)

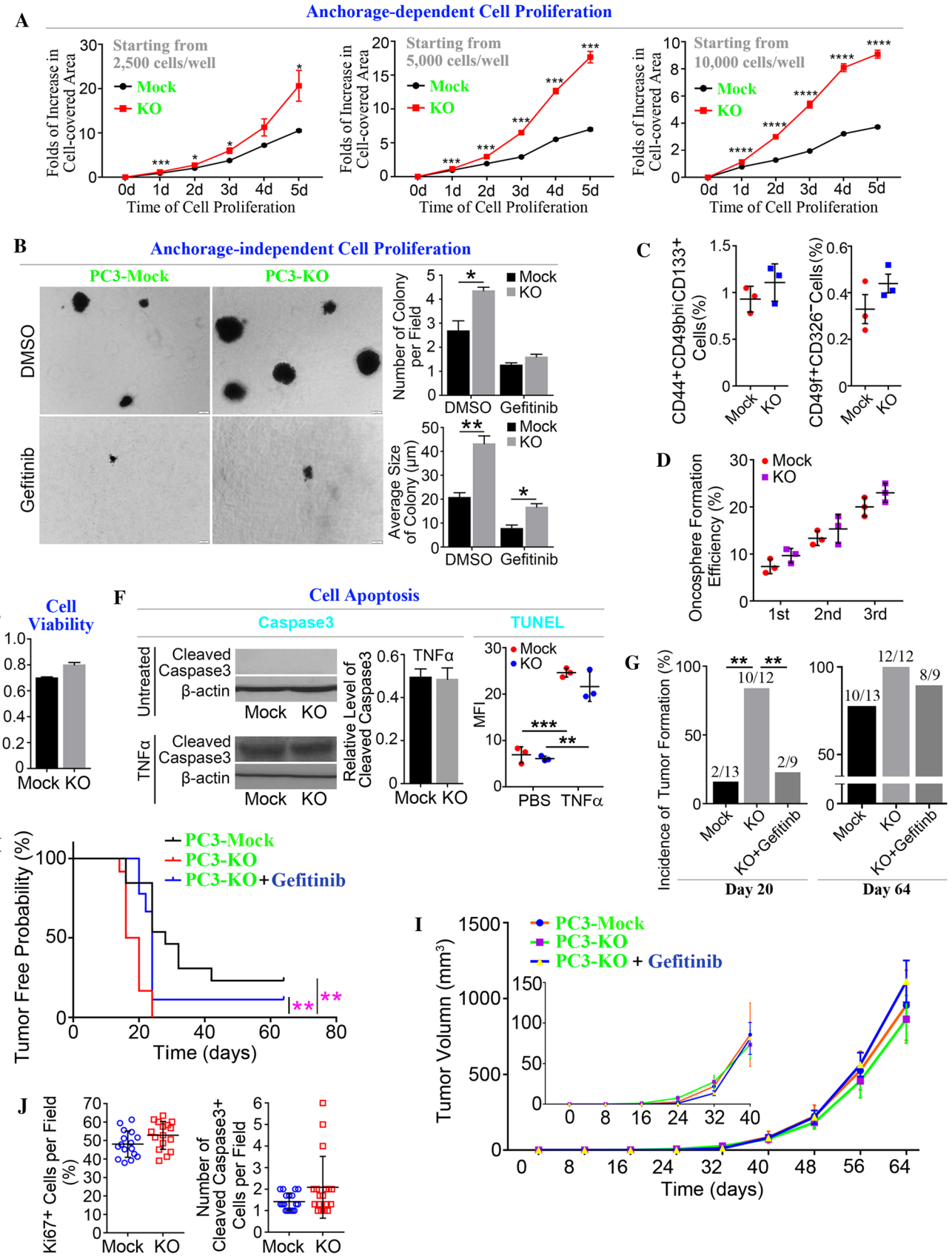
A
Anchorage-dependent Cell Proliferation
Starting from 2,500 cells/well
Starting from 5,000 cells/well
Starting from 10,000 cells/well
Mock
KO
Folds of Increase in Cell-covered Area
Time of Cell Proliferation
0d 1d 2d 3d 4d 5d
B
Anchorage-independent Cell Proliferation
PC3-Mock
PC3-KO
DMSO
Gefitinib
Number of Colony per Field
Average Size of Colony (μm)
C
CD44+CD49bhiCD133+ Cells (%)
CD49f+CD326− Cells (%)
D
Oncosphere Formation Efficiency (%)
1st 2nd 3rd
E
Cell Viability
OD Value
F
Cell Apoptosis
Caspase3
TUNEL
Untreated
TNFα
Cleaved Caspase3
β-actin
Relative Level of Cleaved Caspase3
MFI
PBS TNFα
G
Incidence of Tumor Formation (%)
2/13 10/12 2/9
10/13 12/12 8/9
Mock KO KO+Gefitinb
Day 20
Day 64
H
PC3-Mock
PC3-KO
PC3-KO+Gefitinib
Tumor Free Probability (%)
Time (days)
I
PC3-Mock
PC3-KO
PC3-KO + Gefitinib
Tumor Volumn (mm3)
Time (days)
J
Ki67+ Cells per Field (%)
Number of Cleaved Caspase3+ Cells per Field
Mock KO

◂**Fig. 2** EWI2 removal promotes tumor cell proliferation and tumor formation. **A** Proliferations of PC3-Mock and -KO cells on culture plates were examined with Incucyte System as described in Materials&Methods, at different starting cell densities, and quantified for the changes in cellular areas in the plated (mean ± SD, $n=3$ individual experiments) on a daily basis. *$p<0.05$ and ***$p<0.001$. **B** Anchorage-independent cell proliferation was examined with soft-agar assay as described in Materials&Methods and quantified as number and size of colonies per microscopic field (mean ± SD, $n=3$ individual experiments). *$p<0.05$ and **$p<0.01$. **C** Oncospheres were formed after the cells were cultured in tumorsphere medium for 10 days, imaged with light microscope, and quantified as oncosphere formation efficiency (mean ± SD, $n=3$ independent experiments). **D** Cancer stem cell populations were examined by flow cytometry with the combinations of the indicated prostate cancer stem cell markers and presented as percentage of total cells (mean ± SD, $n=3$ independent experiments). **E** Cell survival was examined with CCK8 assay as described in Materials&Methods and quantified as OD values (mean ± SD, $n=3$ individual experiments with triplicate per group in each experiment). **F** For apoptosis analysis, the cells were treated with TNF-α (20 ng/ml) for 48 h and lysed, and cleaved Caspase3 was examined by Western blot and quantified as relative levels of normalized band densities (mean ± SD, $n=3$ independent experiments). Or cells were stained with TUNEL after TNF-α treatment and detected by flow cytometry. MFI was presented as mean ± SD ($n=3$ independent experiments). **G** Tumor formation after subcutaneous injection of PC3-Mock and -KO cells into nude mice, in the absence or presence of gefitinib, which was administered orally at 500 mg/kg of mouse body weight at 1, 2, 3, 5, and 7 weeks after tumor cell injection. Incidence of tumor formation is calculated at 20th day and 8th week, respectively. **$p<0.01$. **H** Tumor-free probability, based on the experiments described in **G**, is assessed as percentage of mice carrying no tumor. **$p<0.01$. **I** Growth of primary tumors formed by PC3-Mock and -KO cells, in the presence of Gefitinib, as described in **G**. **J** Primary tumors were stained with Ki67 and cleaved Caspase 3 antibodies, respectively. Percentage of Ki67+ cells and number of cleaved Caspase 3+ cells in each randomly selected field were measured by Image **J**, presented as mean ± SD

primary tumors formed by PC3-EWI2 KO cells in nude mice (see below), compare to those by PC3-Mock cells (Fig. 1E), suggesting that PC3-EWI2 KO tumors are more mesenchymal and thereby more invasive. Further examination showed that, for hematogenous dissemination of PC3 cells after tail vein injection in experimental metastasis assay, both incidence and number of micro-metastatic lesions in the lungs were apparently increased in PC3-KO group, compared to PC3-Mock group, although no visible or macro-metastatic lesion was found in the lungs of both groups (Fig. 1H), consistent with more aggressive behaviors of PC3-KO cells in vitro.

## EWI2 inhibits anchorage-independent and -dependent proliferation of tumor cells

Because (i) cell adhesion proteins and growth factor receptors in TMEDs regulate both cell movement and cell proliferation and (ii) EWI2 as a TMED component likely affects both cell movement and cell proliferation, we then evaluated the effect of EWI2 removal on tumor cell proliferation and survival. EWI2 KO markedly elevated the pace of PC3 cell proliferation when the cells were cultured on 2D dishes (Fig. 2A), analyzed by Incucyte Imaging System. EWI2 KO also accelerated the cell proliferation when the cells grew in 3D soft agar, assessed by the size of colony, and promoted the colony formation, assessed by the number of colonies, indicating that EWI2 removal potentiates the malignancy of tumor cells and supports anchorage-independent proliferation (Fig. 2B). The populations of tumor initiating cells or tumor stem cells, reported by their markers $CD49f^{+}CD326^{-}$ [30] and $CD44^{+}CD49b^{hi}CD133^{+}$ [31], remained at similar levels between PC3-Mock and PC3-KO cells (Fig. 2C), so were the formation efficiencies of primary, secondary, and tertiary tumorspheres (Fig. 2D), underlining that EWI2 removal does not promote dedifferentiation of PC3 cells. EWI2 KO did not change PC3 cell survival, evaluated by CCK8 assay (Fig. 2E), and had no impact on apoptosis either at basal level or induced by TNF-α (Fig. 2F).

To evaluate the role of EWI2 in vivo, we inoculated NU/J nude mice subcutaneously with the PC3 transfectant cells. More mice with PC3-EWI2 KO cells formed tumor than the ones with PC3-Mock cells (Fig. 2G). Furthermore, the PC3-EWI2 KO group formed palpable tumor masses much earlier than the PC3-Mock group, as all of PC3-EWI2 KO mice formed tumor within 20 days after inoculation (Fig. 2H). But the tumors grew comparably between the two groups (Fig. 2I). We further examined Ki67 and cleaved Caspase-3, which reflect proliferation and apoptosis, respectively, in primary tumor tissues and found no obvious difference between two groups (Figs. 2J and S2C).

## EWI2 removal leads to partial EMT

EWI2 silencing markedly upregulated the surface level of fibronectin-binding integrin α5 and downregulated that of laminin-binding integrin α6 (Fig. 3A), suggesting elevated function of mesenchymal integrin and diminished function of epithelial integrin. Indeed, cell adhesion onto FN was increased while adhesiveness to LN111 was decreased, upon EWI2 removal (Fig. 3A). EWI2 ablation also elevated the cell surface level of CD44, an invasiveness-promoting cell adhesion protein and an EMT marker (Fig. 3B).

As EMT typically couples with reduced cell–cell adhesion, we investigated the effect of EWI2 removal on cell–cell adhesion proteins. E- and N-cadherin protein levels were unaltered upon EWI2 removal, but EWI2 silenced PC3 cells tended to be compromised in forming mature or close

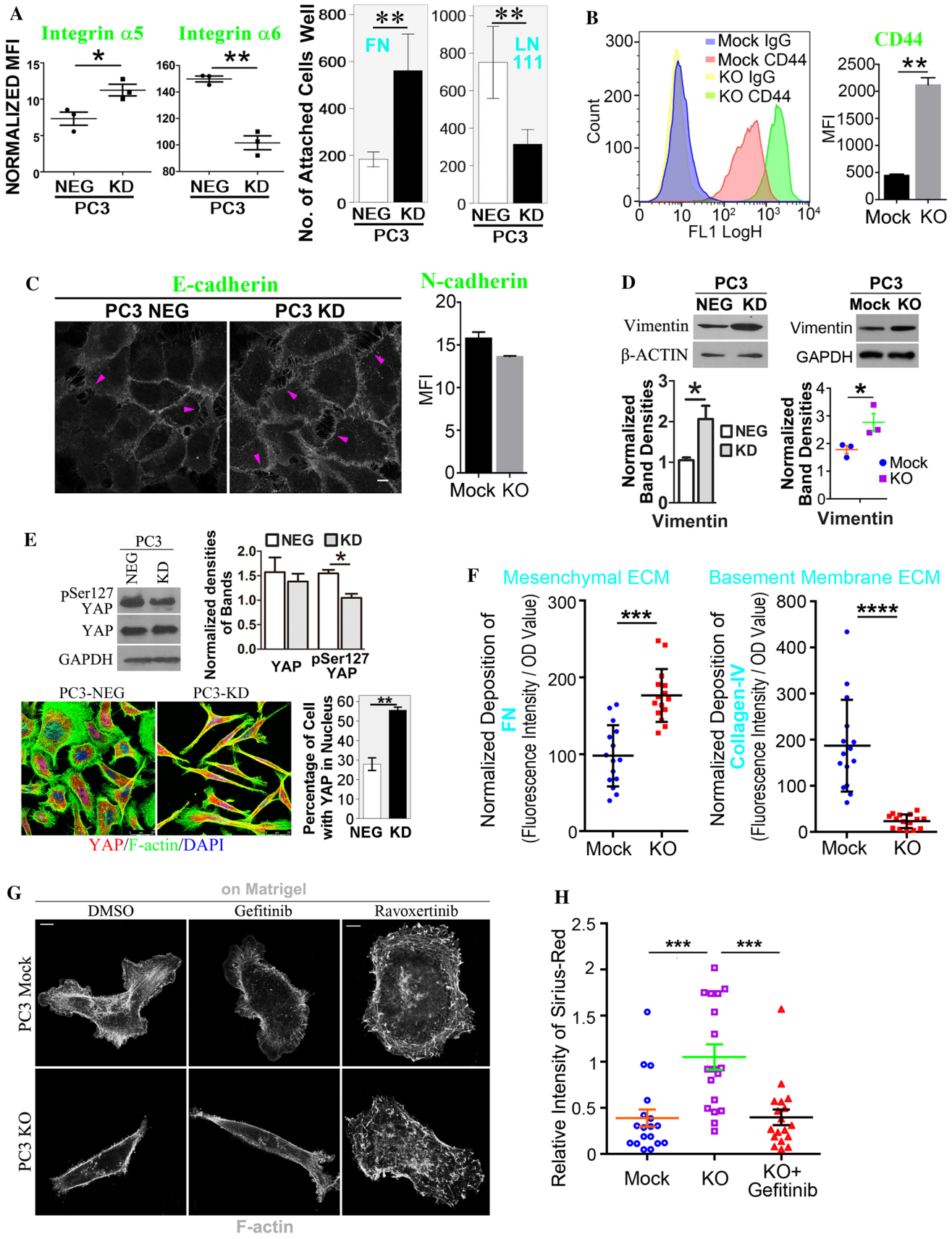
A
Integrin α5
Integrin α6
NORMALIZED MFI
NEG KD
PC3
No. of Attached Cells Well
FN
LN 111
B
Mock IgG
Mock CD44
KO IgG
KO CD44
Count
FL1 LogH
CD44
MFI
Mock KO
C
E-cadherin
PC3 NEG
PC3 KD
N-cadherin
MFI
Mock KO
D
PC3
NEG KD
Vimentin
β-ACTIN
GAPDH
Normalized Band Densities
Mock
KO
E
pSer127 YAP
YAP
GAPDH
Normalized densities of Bands
PC3-NEG
PC3-KD
Percentage of Cell with YAP in Nucleus
YAP/F-actin/DAPI
F
Mesenchymal ECM
Basement Membrane ECM
Normalized Deposition of FN
Normalized Deposition of Collagen-IV
(Fluorescence Intensity / OD Value)
G
on Matrigel
DMSO
Gefitinib
Ravoxertinib
PC3 Mock
PC3 KO
F-actin
H
Relative Intensity of Sirius-Red
KO+ Gefitinib

◂**Fig. 3** EWI2 removal facilitates EMT of PC3 prostate cancer cells. **A** Cell surface integrin levels and cell–matrix adhesion. Integrin α5 and α6 expressions upon EWI2 KD were analyzed by flow cytometry and are presented as MFI (mean ± SD, $n = 3$ independent experiments) on the left. Cell adhesion onto FN (10 μg/ml) or LN111 (50 μg/ml) was performed as described in Materials and Methods. Adhesiveness is presented as the number of attached cells per well (mean ± SD, $n = 3$ individual experiments) on the right. $^{*}p < 0.05$, $^{**}p < 0.01$. **B** Cell surface levels of CD44 upon EWI2 KO were analyzed by flow cytometry and are presented as MFI (mean ± SD, $n = 3$ independent experiments). $^{**}p < 0.01$. **C** Cell–cell adhesion was examined in control and EWI2-silenced PC3 cells in the hanging-drop cell aggregation assay, with or without $Ca^{2+}$ presence, as described in Materials&Methods. Cell–cell adhesiveness was quantified as the area of aggregates (mean ± SD, $n = 3$ independent experiments). $^{**}p < 0.01$. $^{***}p < 0.001$. E-cadherin distribution was revealed by immunofluorescence, and digitation junctions indicated by pink arrowheads (Middle). N-cadherin levels at the cell surface were measured by flow cytometry (Right). **D** Western blot analysis on vimentin. The band densities of vimentin were quantified, normalized by those of actin or GAPDH, and then presented as mean ± SD ($n = 3$ individual experiments). $^{*}p < 0.05$. **E** Western blot analysis on total and $Ser^{127}$-phosphorylated YAP and immunofluorescence analysis on nuclear translocation of YAP. The band densities and numbers of nuclear YAP-positive cells were quantified and presented as mean ± SD ($n = 3$ individual experiments). $^{**}p < 0.01$. $^{***}p < 0.001$. The images were capture by confocal microscopy. Scale bar: 25 μm. **F** ECM deposition of PC3 cells which were cultured on glass coverslips in complete media for 2 days was immune-stained sequentially with primary and secondary Abs, imaged by fluorescence microscopy, and quantified with ImageJ as fluorescence units (see Supplemental Fig. 2D). After normalized by the cell quantities on the glass coverslips (see Supplemental Fig. 2D), the deposited ECMs are presented as relative units (mean ± SD, $n = 3$ individual experiments). $^{***}p < 0.001$ and $^{****}p < 0.0001$. **G** The cells were cultured on Matrigel, fixed, stained with Alexa488-conjugated phalloidin, and imaged by fluorescence microscopy. Scale bar: 10 μm. **H** Tumor tissues formed on mice (6 mice in each group) were stained by Sirius Red. 3 random sections were processed in each tumor tissue. The intensity of Sirius red of each section was measured by ImageJ, compared by *t*-test and shown as mean ± SD. $^{***}$ $p < 0.001$

cell–cell contacts and were stalled at the stage of digitation junction (Fig. 3C), [32] supporting that EWI2 removal facilitates cell dissociation from each other or EMT.

In addition, intermediate filament component vimentin, another marker of EMT, was also increased upon EWI2 removal (Fig. 3D).

As a component of Hippo signaling regulated by cell–cell contacts, $pSer^{127}$-YAP proteins were markedly reduced upon EWI2 silencing, while total YAP remained unchanged (Fig. 3E). Consistently, nuclear translocation of YAP was elevated in EWI2-silenced cells, suggesting that EWI2 sustains Hippo signaling and supporting that Hippo signaling limits EMT [33].

Deposition of FN, a representative of mesenchymal ECM, was elevated in PC3-KO cells, compared to PC3-Mock cells, while deposition of collagen IV, an epithelial basement membrane ECM, was reduced in PC3-KO cells (Figs. 3F and S2E).

Cell morphology became more mesenchymal or fibroblast-like upon EWI2 removal (Fig. 3E), and such morphology denotes a typical cellular status when Hippo signaling is off [34]. Similarly, more EWI2-silenced PC3 cells exhibit mesenchymal morphology on collagen-I gel (data not shown) or Matrigel (Fig. 3G), which more mimics in vivo conditions. Furthermore, tumors formed by PC3 cells in nude mice (see below) contained much more collagenous fibers, as shown by SiriusRed staining, in EWI2 KO group, than the Mock group (Figs. 3F and S2D).

To this end, these observations collectively underline that EWI2 prohibits mesenchymal properties and EWI2 removal promotes mesenchymal movement of tumor cells.

## EWI2 prevents partial EMT by confining EGFR-Erk signaling

To determine how EWI2 silencing leads to the mesenchymal modes of cell movement, we examined the role of EGFR/MEK/Erk signaling in EWI2 function, since tetraspanin-enriched membrane domains (TEMDs) crosstalk with EGFR [6]. After EWI2 KD or KO, EGFR/MEK/Erk signaling was markedly upregulated, with (1) more total and $Tyr^{1068}$-phosphorylated EGFRs, (2) higher levels of MEK1 and/or MEK2 proteins, and (3) increased Erk phosphorylation or activation (Fig. 4A). All changes indicate elevated EGFR signaling upon EWI2 KD.

Interestingly, accumulations of EGFRs in cytoplasmic vesicles (Fig. 4B, left panel) were observed in EWI2-silenced PC3 cells, consistent with less presence of EGFR at the cell surface (right panel in Fig. 4B). Consistently, EGFR internalization, induced and probed by its ligand EGF, was elevated upon EWI2 silencing (Fig. 4C).

To determine how EWI2 restrains EGFR activation, we analyzed the EGFR distribution in PC3 cells by super-resolution imaging. Figure 4D shows (i) representative images of dSTORM super-resolution fluorescence (left panel) and (ii) single particle localizations determined from regions of interest (ROIs) (right panel). Single particle localizations are color coded to denote their assignment to different cluster sizes from the DBSCAN analysis.

From the clustering analyses on dSTORM data, we found that PC3-KD cells had much higher density of clusters than PC3-NEG cells (Fig. 4E, left panel). The number of localizations per ROI (Fig. 4E, middle panel) and fraction of clustered localizations (Fig. 4E, right panel) were also markedly increased in PC3-KD cells, compared to PC3-NEG cells. The sizes or radii of the clusters exhibited a moderate increase in PC3-KD cells, as shown by the cumulative distribution function plot (Fig. 4F). There were no obvious trends among the conditions for compactness ($4\pi A/P^2$, where A and P denote the area and perimeter of the cluster, respectively) between the two groups. Hence, clustering of

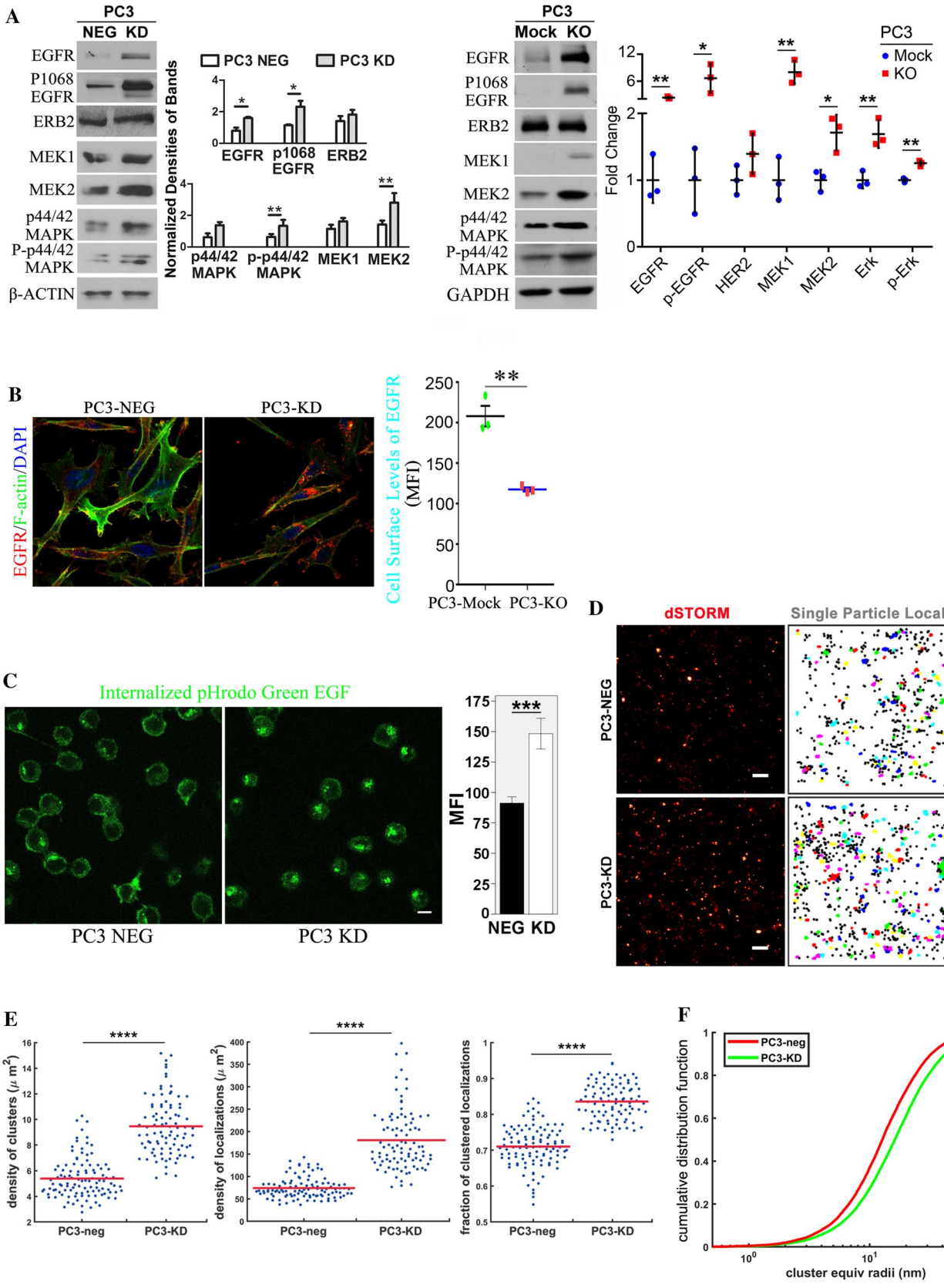
A
PC3
NEG KD
EGFR
P1068 EGFR
ERB2
MEK1
MEK2
p44/42 MAPK
P-p44/42 MAPK
β-ACTIN
PC3 NEG
PC3 KD
Normalized Densities of Bands
EGFR
p1068 EGFR
ERB2
p44/42 MAPK
p-p44/42 MAPK
MEK1
MEK2
PC3
Mock KO
GAPDH
Fold Change
PC3
Mock
KO
EGFR
p-EGFR
HER2
MEK1
MEK2
Erk
p-Erk
B
PC3-NEG
PC3-KD
EGFR/F-actin/DAPI
Cell Surface Levels of EGFR (MFI)
PC3-Mock PC3-KO
C
Internalized pHrodo Green EGF
PC3 NEG
PC3 KD
MFI
NEG KD
D
dSTORM
Single Particle Localization
PC3-NEG
PC3-KD
E
density of clusters (μ m²)
density of localizations (μ m²)
fraction of clustered localizations
PC3-neg
PC3-KD
F
PC3-neg
PC3-KD
cumulative distribution function
cluster equiv radii (nm)

◂**Fig. 4** EWI2 removal potentiates EGFR-MAPK signaling by increasing endosomal retention and surface clustering of EGFR. **A** The components of the EGFR/MEK/ERK signaling pathway were analyzed with Western blot in PC3 KD (left) and KO (right) transfectant cells, together with actin and GAPDH as loading controls of whole cell lysates. The proteins were quantified as band densities and presented as relative levels (mean ± SD, $n = 3 \sim 4$ individual experiments). $*p < 0.05$ and $**p < 0.01$. **B** Steady-state distribution of EGFR in PC3-NEG and -KD cells. After the cells were fixed, permeabilized, and stained for EGFR with EGFR mAb, F-actin with phalloidin, and nucleus with DAPI, immunofluorescence images were captured with confocal microscopy. (left) The cell surface expression levels of EGFR were measured via flow cytometry and presented as mean ± SD ($n = 3$ independent experiments). $**p < 0.01$. **C** EGFR endocytosis. PC3-NEG and -KD cells were incubated with pHrodo Green EGF at 37 °C for 15 min, fixed, and imaged with confocal microscopy. Scale bar: 10 μm. The internalized EGF was quantified as fluorescence intensity (mean ± SD, $n = 3$ independent experiments) with ImageJ software and analyzed via independent samples $t$ test. $***p < 0.001$. **D** EWI2 removal results in more and larger EGFR clustering at the cell surface. The cells were treated with EGF (25 nM) for 2 min, fixed, and stained with Alexa647-conjugated EGFR Ab. The EGFR distribution on the cell surface was imaged at nano-scale by dSTORM super-resolution microscopy, and representative images are shown on the left panel. Representative images for clusters identified by DBSCAN analysis are shown on the right panel. Scale bars: 500 nm. **E** Clustering analysis results for pooled data from multiple "regions of interest" (ROIs) on 12 different cells for each condition. Mean values are indicated by red lines, and p values for the panels from left to right are $1.38e^{-28}$, $1.72e^{-30}$, and $2.49e^{-28}$, respectively. **F** Cumulative distribution function (CDF) plot shows the sizes (radii) of the EGFR clusters. Twelve individual cells were examined for each group, and multiple ROIs for each cell

EGFR at or near the cell surface was markedly increased upon EWI2 removal.

## EWI2 upholds EGFR at cell surface

To determine the mechanism responsible for more EGFR endocytosis upon EWI2 removal, we examined EWI2 effect on endocytic routes of EGFR. As EGFR undergoes clathrin- and caveolin-dependent endocytoses [35–37], Western blot analysis revealed that the level of clathrin heavy chain (CHC), which reports clathrin endocytic route, remained unchanged while caveolin-1 and cavin1, both crucial for caveola-dependent endocytosis, were up-regulated, upon EWI2 ablation (Fig. 5A). Steady-state colocalizations of EGFR with CHC and caveolin1 were both increased in PC3-EWI2 KO cells, compared to PC3-Mock cells, if we take both M1 and M2 into consideration (Fig. 5B). Increased colocalizations occurred mainly in peri-nuclear regions, suggesting their more co-existence in late endosomal and/or biosynthetic compartments. Using fluorescently labeled EGF as the probe for EGF endocytosis, we found that internalized EGF entered both clathrin- and caveolin-positive compartments and EWI2 KO enhanced EGF endocytosis into both compartments (Fig. 5C) if we take more caveolin1 and internalized EGF into consideration (Figs. 4C and 5A), indicating that EWI2 constrains both clathrin- and caveolin1-mediated endocytoses of EGF. This endocytosis assay, however, has a caveat as the pHrodo-EGF probe becomes only fluorescent under low pH environment. Hence, no or few colocalization of caveolin1 with pHrodo-EGF (Fig. 5C) could be due to relatively higher pH in caevolin1 endocytic compartment. To circumvent this potential hurdle, we used EGFR mAb as the probe to trace EGFR endocytosis. The internalized EGFR indeed displayed low but comparable levels of colocalization with caveolin1 in both groups, as shown by Manders colocalization coefficients (Fig. 5D). But, because both internalized EGFR and caveolin1 are increased upon EWI2 ablation, total quantity of internalized EGFR that are colocalized with caveolin1 became markedly increased in the EWI2 KO cells, compared to the Mock cells (Fig. 5D), strongly suggesting that EWI2 removal bolsters EGFR endocytosis through caveolin1-containing/-mediated trafficking route.

Earlier study showed EWI2 inhibits TGFβR signaling in melanoma cells by sequestering CD9/CD81 from TGFβRs and then preventing TGFβRs from clustering for their activation [38]. To determine the contributions of other tetraspanins, we examined CD9 as example using CD9 mAb C9BB to report homo-clustered CD9 and CD9 mAbs ML13, MAB7, and ALB6 to report total CD9 [39]. In total cell lysates homo-clustered CD9 proteins were unchanged but total CD9 were decreased upon EWI2 KO (Fig. 6A), but at the cell surface both homo-clustered and total CD9 levels were markedly reduced upon either EWI2 KD or EWI2 KO (Figs. 6B and S3A, B).

Colocalization analysis on EGFR and CD9 revealed that EGFR-colocalized CD9, either total or homo-clustered CD9, became more upon EWI2 removal, while total CD9-colocalized EGFR, not homo-clustered CD9-colocalized EGFR, were decreased in EWI2-KO cells (Fig. 6C). This observation strongly suggests that more CD9 proteins are present nearby EGFR upon EWI2 removal. Taken more EGFR but comparable homo-clustered CD9 in PC3-KO cells into consideration, this observation also suggests that more homo-clustered CD9 proteins are present nearby EGFR upon EWI2 removal. Further analysis on the colocalization between internalized EGF and CD9 also revealed that the EGF-colocalized, homo-clustered CD9 became more upon EWI2 removal (Fig. 6D). The homo-clustered CD9-colocalized EGF remained unchanged upon EWI2 KO (Fig. 6D), indicating that more homo-clustered CD9 are nearby the internalized EGF given the fact of more internalized EGF in PC3-KO cells. Together, these observations underline more homoclustered CD9 are present in close proximity of EGFR and internalized EGF.

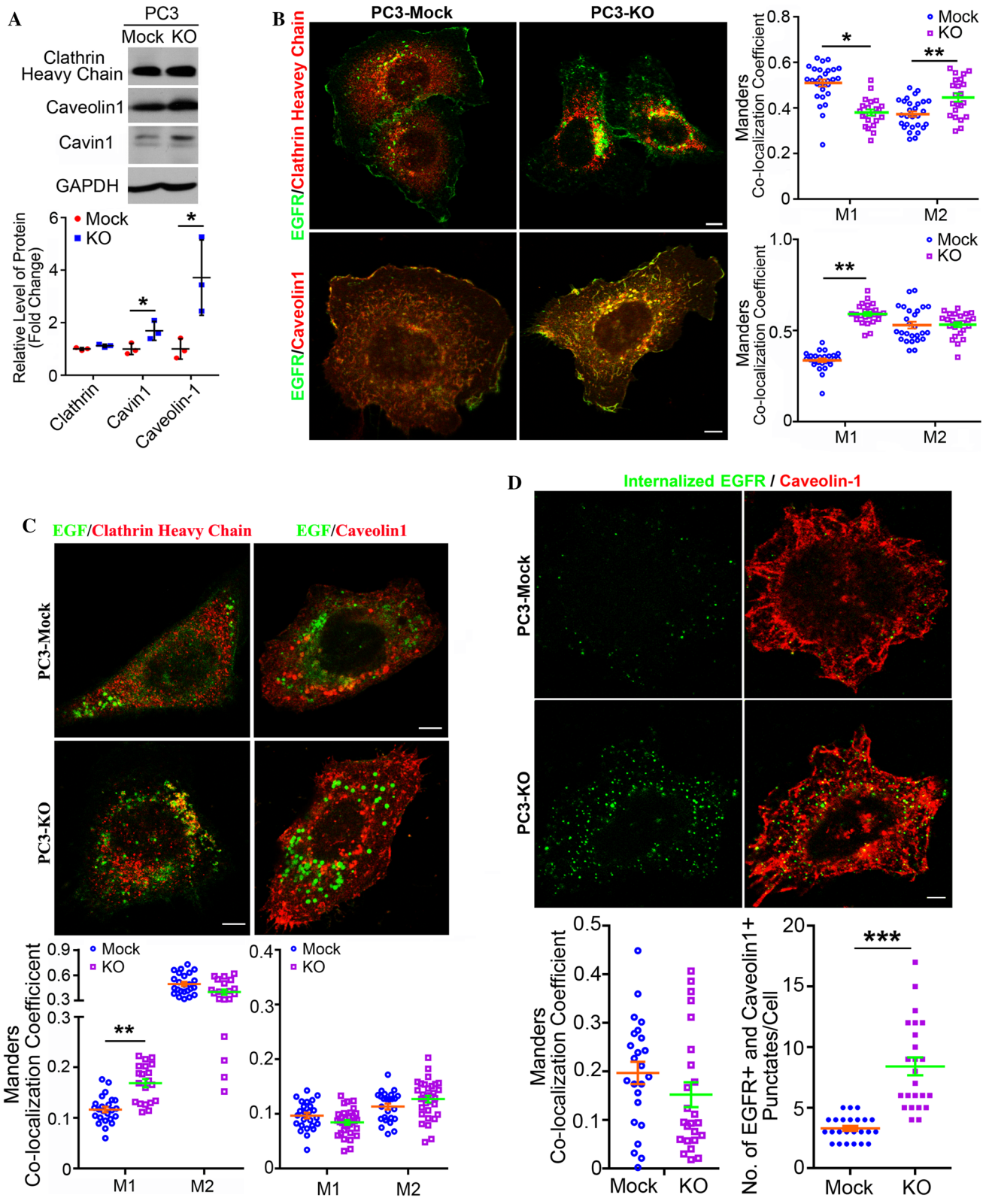


We further examined the impacts of EWI2 removal on CD9 trafficking through clathrin- and caveolin-positive compartments. Colocalization of CHC with total or homo-clustered CD9 was not altered upon EWI2 KO (Figure S4A), as less total CD9-colocalized clathrin can be attributed to less total CD9 in PC3-KO cells.

◂**Fig. 5** EWI2 removal promotes EGFR trafficking through clathrin-mediated endocytosis. **A** Indicated proteins of PC3 transfectant cells were analyzed with Western blot with GAPDH as a loading control of whole cell lysates, quantified as band densities, and presented as relative levels (mean ± SD, $n = 3 \sim 4$ individual experiments). $*p < 0.05$, $**p < 0.01$. **B** EGFR colocalization with CHC or caveolin1 in PC3 transfectant cells at steady state. After the cells were fixed, permeabilized, and stained sequentially with primary and secondary Abs, immunofluorescence images were captured with confocal fluorescence microscopy. Of note, EGFR Ab and CHC or caveolin1 Ab came from different species (See Table S1). EGFR colocalizations with CHC and caveolin1 were presented as Manders coefficients (mean ± SE, $n = 3$ independent experiments, and $7 \sim 9$ cells were analyzed per experiment). M1 = EGFR-colocalized CHC/CHC or EGFR-colocalized caveolin1/caveolin1, and M2 = CHC-colocalized EGFR/EGFR or caveolin1-colocalized EGFR/EGFR. $*p < 0.05$, $**p < 0.01$. Scale bars: 10 μm. **C** Colocalization of internalized EGF with CHC or caveolin1. PC3-Mock and -KO cells were incubated with pHrodo Green EGF at 37 °C for 30 min, fixed, and imaged with confocal microscopy. Scale bar: 10 μm. The colocalizations of internalized EGF with CHC and caveolin1 were presented as Manders coefficients (mean ± SE, $n = 3$ independent experiments, and $7 \sim 9$ cells were analyzed per experiment). M1 = EGF-colocalized CHC/CHC or EGF-colocalized caveolin1/caveolin1, and M2 = CHC-colocalized EGF/EGF or caveolin1-colocalized EGF/EGF. $*p < 0.05$. Scale bars: 6 μm. **D** Cells were incubated with EGFR mAb (GFR450, 2 ug/ml) at 37 °C for 30 min, washed with PBS three times, fixed by 4% PFA at room temperature for 10 min, permeabilized by 0.1% Triton X-100 at room temperature for 5 min, and incubated sequentially with caveolin-1 pAb at 4 °C overnight and secondary Ab at room temperature for 1 h. Images were taken under Leica SP8 confocal microscope and analyzed by ImageJ. Data are presented as mean ± SE ($n = 24$ individual cells). $***p < 0.001$

Colocalizations of caveolin1 with total and homo-clustered CD9 were both increased upon EWI2 removal (Figure S4B), as less total CD9-colocalized caveolin1 can be attributed to less total CD9 and more caveolin1 in PC3-KO cells. These observations suggest that EWI2 removal enhances CD9 partition to and/or trafficking through caveolin1-containing compartment. Interestingly, the patterns of colocalization coefficients of CD9 and caveolin1 are identical to the ones of CD9 and EGFR (Figs. 6C and S4B).

Besides PC3 cells, the inverse correlation between EWI2 expression and cell motility can also be observed in Du145 human prostate cancer cells. Silencing EWI2 in Du145 cells resulted in elevated invasiveness (Fig. 7A, B). Consistently, gross upregulation of EGFR-Erk signaling was also observed in EWI2-silened Du145 cells (Fig. 7C).

Collectively, the findings above support an inverse correlation between EWI2 and EGFR-Erk signaling. Notably, the EGFR inhibitor Gefitinib and Erk inhibitor Ravoxertinib reduced the increased invasiveness through Matrigel of EWI2-silenced PC3 cells (Fig. 1F) and the elevated migration on collagen-I gel of PC3 cells (Fig. 1G) to levels comparable with those of the control cells. Ravoxertinib also abrogated the formation of micro-metastatic lesions in lung of PC3-KO cells through tail veins, in experimental metastasis assay (Fig. 1H). Similar effects of Gefitinib and Ravoxertinib on invasion were also observed in EWI2-silenced Du145 cells (Fig. 6B). Gefitinib also abolished the difference in oncogenic colony formation between the two groups in vitro (Fig. 2B) and postponed tumor initiation of nude mice carrying tumors formed by EWI2-ablated PC3 cells (Fig. 2H). Furthermore, Ravoxertinib converted the mesenchymal or fibroblast-like morphology of PC3-EWI2 KO cell to cobblestone-like morphology, although Gefitinib did not (Fig. 3G), and Gefitinib reduced fibrotic or mesenchymal property of the tumor formed by PC3-EWI2 KO cells (Figs. 3G and S2E). These observations strongly suggest that elevated EGFR signaling contributes to EWI2 removal-induced i) increase in malignancy of tumor cells and ii) partial EMT.

### EWI2 gene expression and human prostate cancer

Since EWI2 inhibits (i) outside-in signaling in prostate cancer cells and (ii) prostate cancer xenograft in mice, we investigated the impact of EWI2 gene expression on human PRAD (Figure S5). EWI2 gene expression cannot predict the patient prognosis, despite a moderate increase in PRAD and a marginal negative correlation with PSA level (Fig. S5A–D). But in a very small portion of PRAD patients, EWI2 gene is extensively deleted (Fig. S5B). Furthermore, EWI2 gene expression does not correlate strongly with EGFR, HER2, or HER3 gene expressions (Fig. S5E), supporting our observations above that EWI2 down-regulates EGFR at post-translation stages such as endocytosis. Interestingly, among MEK1, MEK2, Erk1, and Erk2, EWI2 displayed impressive correlation with MEK1 and Erk2 in gene expression (Fig. S6E).

## Discussion

### EWI2 functionally interacts with TEMDs: from TEMD reorganization to TEMD trafficking

EWI2 associates with tetraspanins and inhibits tumor cell movement, tumor growth, and tumor metastasis [3, 38]. For example, EWI2 overexpression down-regulates integrin-dependent migration of tumor cells on LN by enhancing tetraspanin CD81-integrin α3β1 association [40] and inhibits collective migration of fibroblasts [29]. Consistently, the EWI2-associated tetraspanins such as CD9, CD81, and CD82 [2, 3] also regulate cell movement [41, 42], probably by altering the activities of their physically associated cell adhesion molecules (CAMs) and growth factor receptors. For example, CD9 affects cell migration by modulating integrin activation [43] and EGFR activity [11, 12].

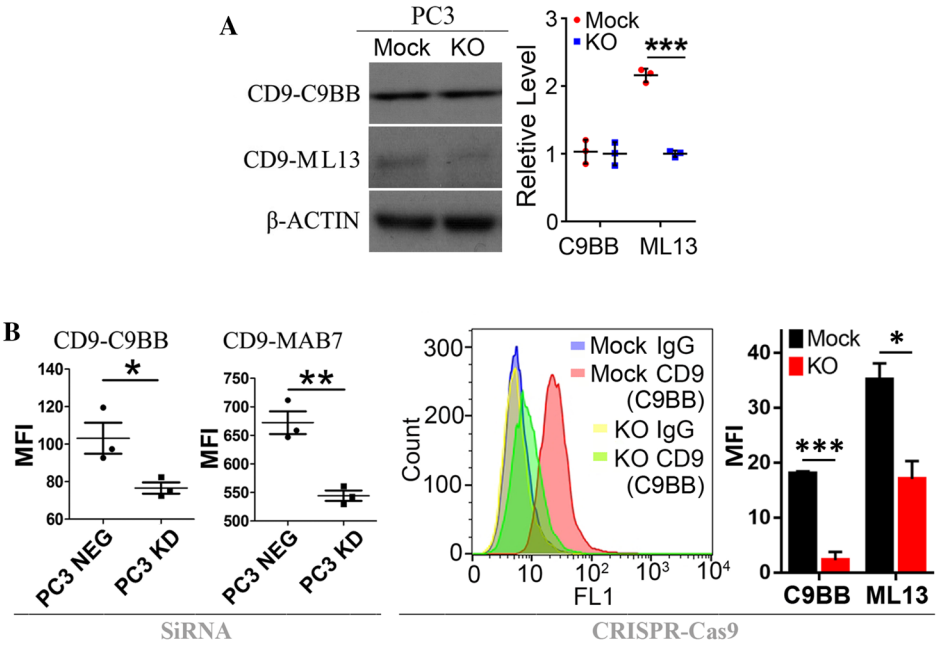
A
PC3
Mock KO
CD9-C9BB
CD9-ML13
β-ACTIN
Reletive Level
Mock
KO
***
C9BB ML13
B
CD9-C9BB
CD9-MAB7
MFI
*
**
PC3 NEG
PC3 KD
SiRNA
Count
Mock IgG
Mock CD9 (C9BB)
KO IgG
KO CD9 (C9BB)
FL1
CRISPR-Cas9
C9BB ML13

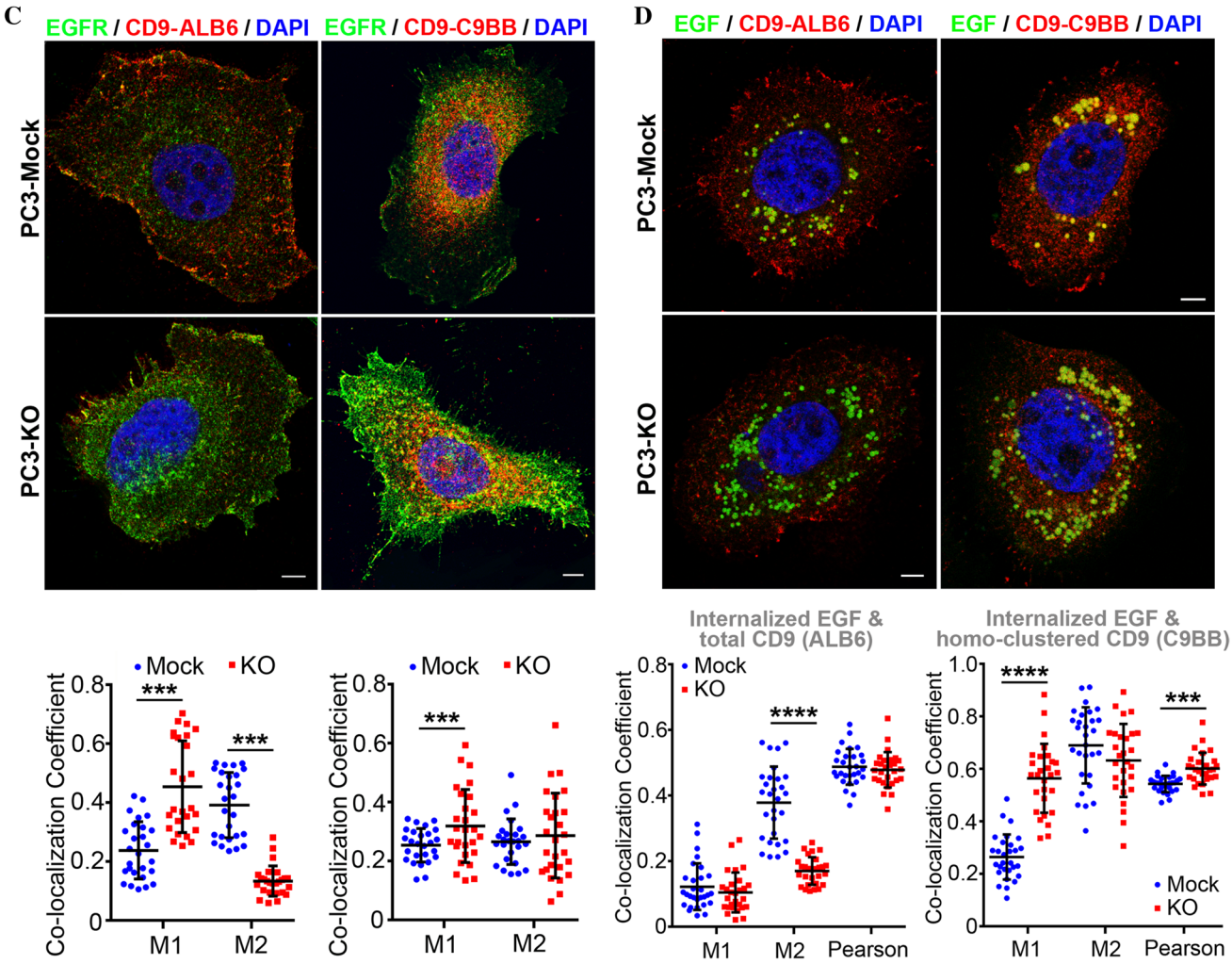
C
EGFR / CD9-ALB6 / DAPI
EGFR / CD9-C9BB / DAPI
PC3-Mock
PC3-KO
D
EGF / CD9-ALB6 / DAPI
EGF / CD9-C9BB / DAPI
Co-localization Coefficient
Mock
KO
M1
M2
Internalized EGF & total CD9 (ALB6)
Internalized EGF & homo-clustered CD9 (C9BB)
Pearson

◂**Fig. 6** Effects of EWI2 removal on CD9 homo-clustering and CD9 interaction with EGFR. Western blot (**A**) and flow cytometry (**B**) analyses on CD9 expression in and on PC3-EWI2 KD and KO cells and their control cells. The levels of CD9 are presented as relative band density (**A**) and MFI (**B**) (mean ± SD, $n = 3$ individual measurements). $*p < 0.05$, $**p < 0.01$, and $***p < 0.001$. Actin serves as a loading control in Western blot (**A**), and isotype-matched IgG staining serves as a negative control in flow cytometry (**B**). Colocalizations of EGFR (**C**) and internalized EGF (i.e., pHrodo Green EGF) (**D**) with total and homo-clustered CD9, stained by CD9 mAbs ALB6 and C9BB, respectively, were examined in immunofluorescence, imaged with confocal microscopy, and quantified as Manders colocalization coefficients (mean ± SD, $n = 3$ individual experiments, nine cells were analyzed per experiment). M1 = EGFR- or EGF-colocalized CD9/CD9, and M2 = CD9-colocalized EGFR or EGF/EGFR or EGF. $***p < 0.001$ and $****p < 0.0001$. Scale bars: 10 μm (**C**) and 8 μm (**D**)

This study expands the mechanistic understanding of EWI2 anti-tumor roles from its regulation on molecular interactions within TEMDs at cell membrane to its regulation on endocytic trafficking of TEMD components like EGFR through endolysosome vesicles. Given that the cytoplasmic domain of EWI2 binds various phosphatidylinositol phosphates in cell membrane [29] and the membrane phosphatidylinositol phosphates play key roles in endocytic trafficking, [44] it is predictive that EWI2 can affect the endocytosis of TEMD components.

Notably, our study also strongly suggests that EWI2 prevents EGFR from interacting caveolin-containing entities, namely caveolae and lipid rafts, and thereby undergoing endocytosis through these endocytic machineries. Given tetraspanins bind cholesterol [32, 45, 46] and lipid rafts enrich cholesterol, whether EWI2 regulates the interactions between TEMDs and lipid rafts becomes an obvious question to be answered in the coming studies.

## EWI2 inhibits tumor cell movement by preventing partial EMT

We found that EWI2 restrains both random and directional solitary movements (migration and/or invasion) of PC3 cells. Directional migration and invasion of the cells are chemo-hepatotactic onto 2D ECMs and through 3D ECMs, respectively, while random migration is under FBS stimulation. Hence, EWI2 restrains the pro-migratory signaling initiated by growth factors and/or ECMs. But increased cell-FN adhesion and decreased cell-LN adhesion upon EWI2 silencing strongly suggest that elevated EGFR signaling is the major driving force for greater movement of EWI2-removed cells. Indeed, EGFR inhibition by Gefitinib and Erk inhibition by Ravoxertinib abolish the increases in invasiveness and migration of EWI2-silenced cells.

During collective cell migration, traction force resulting from cell–matrix adhesion keeps balance with the force derived from cell–cell adhesion, to make the cells not only move but also move together [47–49]. In EWI2-removed cells, greater motile potential due to higher EGFR signaling is possibly offset by poorer motile potential due to lower cell–cell adhesiveness, resulting in no obvious change in collective cell migration. As cell–cell and cell–matrix adhesions crosstalk with each other, [47] the reduced LN adhesion and less basement membrane ECM deposition coincide well with less cell–cell adhesion, when the cells become more mesenchymal.

In PC3 cells, fewer E-cadherin proteins at cell–cell junctions upon EWI2 silencing strongly suggest less cell–cell adhesion and more solitary cell movement. In EWI2-silenced PC3 cells, poorly formed digitation junctions, i.e., microextrusions between cells, [32] support less cell–cell adhesion. More CD44 proteins at cell surface upon EWI2 removal support greater motility potential for PC3 cells. Therefore, when EWI2 is silenced, (i) increased cell-FN adhesion while decreased cell-LN adhesion, (ii) increased deposition of mesenchymal ECM FN while decreased deposition of epithelial ECM collagen-IV, (iii) reduced cell–cell adhesion, and (iv) elevated solitary movement are in accord with mesenchymal transition.

Alternative explanation for the increased movement upon EWI2 removal is the dedifferentiation of tumor cells in the absence of EWI2. As EWI2 removal does not affect the (i) population of tumor initiating/stem/stem-like cells and (ii) formation of tumorspheres, the increased movement is unlikely caused by the dedifferentiation of PC3 cells.

Moreover, this study substantiates the understanding of EWI2 inhibitory effects on prostate cancer cell movement, which have been reported in earlier studies [3, 50]. For example, different from mere investigation of directional solitary migration upon EWI2 overexpression in Du145 prostate cancer cells [3], we systematically analyzed different modes of PC3 prostate cancer cell movement including directional solitary migration, random solitary migration, collective migration, and invasion by EWI2 KD and KO approaches in this study. Different from the report showing that EWI2 inhibits EGFR signaling through exosomal miRNA [50], our study indicates that EWI2 inhibits EGFR signaling through (i) limiting EGFR clustering at the cell surface and (ii) preventing EGFR internalization from caveolin-mediated endocytosis route. In addition, our study (i) elucidates that EWI2 inhibits tumor cell movement by restraining partial EMT, (ii) establishes a causal role between Erk kinase and EWI2 functions in addition to the EWI2-EGFR link, and (iii) reveals the contribution of homo-clustered CD9 to EWI2-mediated inhibition of EGFR.

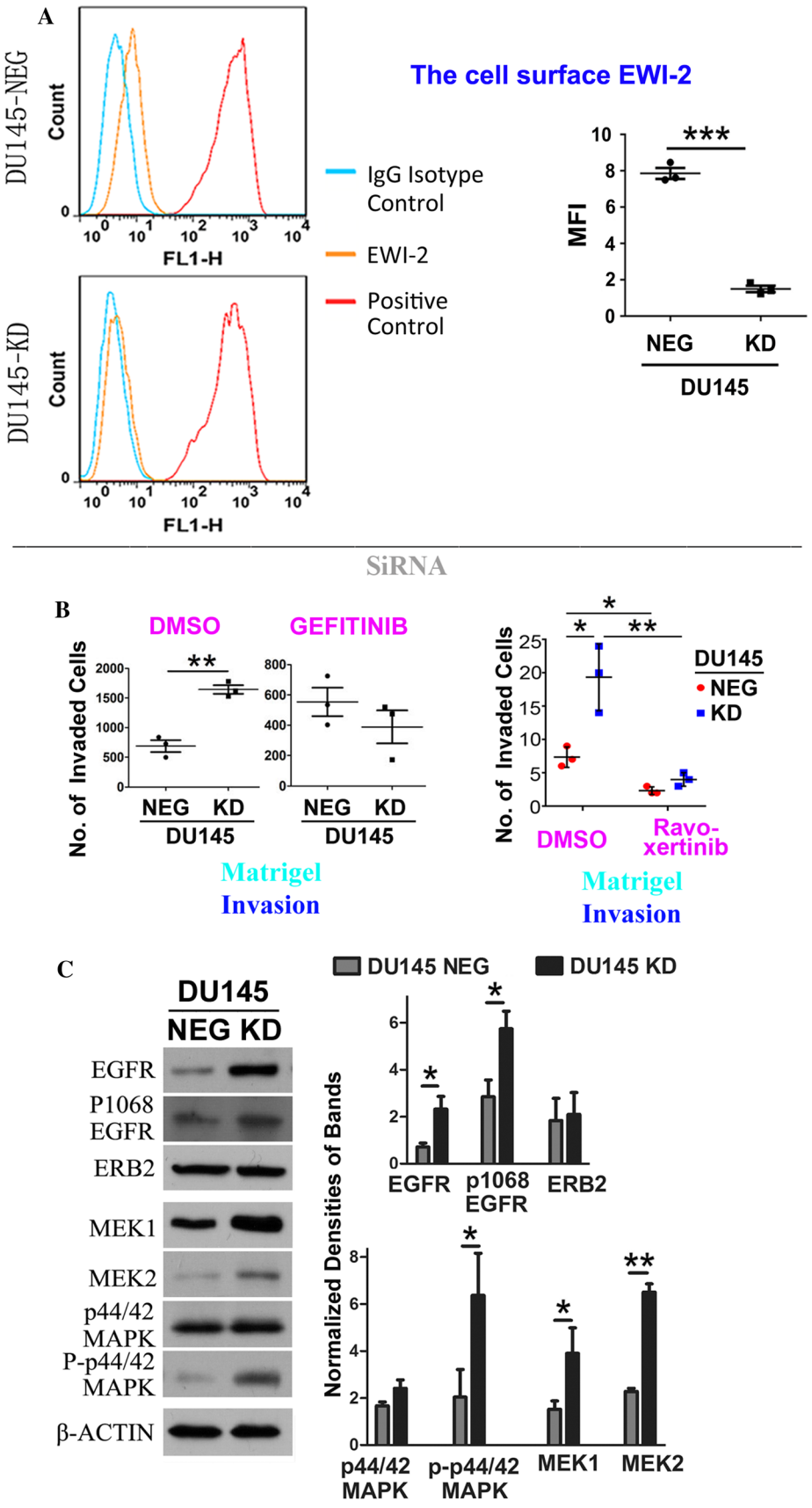


**Fig. 7** Effects of EWI2 KD in Du145 cells on invasiveness and EGFR-Erk signaling. **A** EWI2 expression levels at the cell surface of Du145 cells upon EWI2 KD, as analyzed with flow cytometry and presented as MFI (mean ± SD, $n = 3$ individual measurements). ***$p < 0.001$. Isotype matched IgG staining serves as a negative control. **B** Effects of EGFR and Erk inhibitors on the invasiveness of Du145-NEG and -KD cells through Matrigel. The cells were pre-treated with DMSO or Gefitinib (10μM) for 32 h or Ravoxertinib (1 μM) for 16 h prior to the experiments. Numbers of cells that invaded through the Matrigel were counted and presented as mean ± SD ($n = 3$ independent experiments). *$p < 0.05$ and **$p < 0.01$. **C** The components of the EGFR/MEK/Erk signaling pathway were analyzed with Western blot in Du145 transfectant cells, together with actin as loading control of whole cell lysates. The proteins were quantified as band densities and presented as relative levels (mean ± SD, $n = 4$ individual experiments). *$p < 0.05$ and **$p < 0.01$

### EWI2 restrains EGFR signaling by limiting the cell surface clustering and endocytic trafficking of EGFR

EWI2 KD and KO lead to global upregulation of EGFR-MEK-Erk1/2 signaling, mainly by enhancing the cell surface clustering and endocytosis of EGFR. EWI2 removal enhances both clathrin-mediated and caveolin-mediated endocytoses of EGFR. Earlier study demonstrated that PC3 cells barely contain caveola as the cells do not express cavin [51]. Upregulation of cavin, together with a higher level of caveolin-1, upon EWI2 removal suggest caveola as a viable endocytic route in EWI2-removed cells, in which more EGFR are indeed internalized to caveolin-containing compartment. Even for the cells expressing a negligible amount of or no cavin, caveolin as a lipid raft component could still undergo clathrin-independent but lipid raft-dependent endocytosis. EGFR endocytosis correlates with Erk1/2 activation-dependent transcriptional responses [36, 52], and Erk translocation into the nucleus is needed to promote cell movement [53]. Indeed, nuclear translocation of Erk becomes increased upon EWI2 removal (our unpublished data).

Although our study revealed that EWI2 restrains EGFR signaling by inhibiting EGFR clustering at the plasma membrane and EGFR endocytosis from the plasma membrane, how EWI2 restrains the signaling at and from the plasma membrane, e.g., EGFR clustering, remains to be investigated. In melanoma, EWI2 inhibits TGFβR signaling by sequestering CD9 and CD81, dissociating them from TGFβR1 and TGFβR2, and subsequently preventing TGFβR1-TGFβR2 clustering [38]. For EGFR, EWI2 removal promotes spatial proximity of CD9, especially homo-clustered CD9, with EGFR and internalized EGF in PC3 cells. Hence, consistent with the functional crosstalk between EWI2 and TGFβR [38], EWI2 restraint of EGFR signaling could depend on its sequestration of CD9. Notably, our study strongly suggests that homo-clustered CD9 escorts or facilitates ligand-induced endocytosis of EGFR and that EWI2 insulates homo-clustered CD9 from interacting with EGFR to prevent EGFR endocytosis.

Elevated EGFR-Erk signaling upon EWI2 removal could attribute in part to the altered integrins, as integrins and EGFR can associate physically with each other and share similar signaling downstream [54]. Especially, given that EWI2 is a TEMD component and TEMDs bridge integrins and EGFR [55], it is plausible to predict that integrins contribute to EWI2-altered EGFR activity and signaling. While some EWI2-regulated cellular functions such as random cell migration likely result mainly from changed integrins in EWI2-removed cells. Partial EMT could be another phenotype largely due to the changes in integrins and cellular functions directly controlled by integrins.

In summary, our study reveals that EWI2 inhibits (i) various modes of movement and (ii) proliferation of prostate cancer cells by confining EGFR-Erk signaling, to slow down tumor formation and metastasis. At the molecular level, EWI2 limits (i) formation of larger clusters of EGFR at the cell surface and (ii) endocytic trafficking of EGFR, to prevent EGFR over-activation. Resonating the restraint role of EWI2 in EGFR-Erk signaling, EGFR and Erk inhibitors reduce the elevated movement and proliferation of prostate cancer cells caused by EWI2 removal.

TMED components like tetraspanins and integrins can exert context- and lineage-dependent activities on cancer cell behaviors [56, 57]. We also realize that EWI2 as a TMED component plays differential roles in regulating some cancer cell functions such as proliferation. The effects of EWI2 on PC3 and Du145 prostate cancer cells are largely similar. For example, (i) invasion and directional migration and (ii) EGFR-Erk signaling are elevated in both PC3 and Du145 cells upon EWI2 removal. Although PC3 and Du145 cells reflect the complexity of prostate cancer, the observations from this study underlines the commonality of different prostate cancer cell lines in response to EWI2 removal.

**Supplementary Information** The online version contains supplementary material available at https://doi.org/10.1007/s00018-022-04417-9.

**Acknowledgements** We thank Drs. Felipe V. Catalan and Shoshana Levy of Stanford University for providing EWI2 CRISPR/Cas9 KO system and comments, Ms. Kathy Kyler for English editing, the OMRF imaging facility for image acquisition and analysis, and OUHSC Stephenson Cancer Center tissue pathology core and functional genomics core facility.

**Author contributions** CF, JW, and SP performed experiments, analyzed data, and wrote manuscript. JDW and K-KW analyzed data. YD, JC, and YY performed experiments. HK and MJ provided technical advice. AM and TT provided special reagent and/or technical advice. KAL designed experiments and analyzed data. XAZ designed experiments, analyzed data, and wrote manuscript.

**Funding** This work was supported by OCAST grants HR13-207 and HR20-055, the research grants from OCASCR (a program of TSET), and the University of Oklahoma Health Science Center to XAZ. XAZ is an Oklahoma TSET Cancer Research Scholar.

**Data availability statement** The data that support the findings of this study are available from the corresponding author upon reasonable request.

## Declarations

**Conflict of interest** The authors declare no competing financial interests.

**Ethics statement** All procedures involving animals were performed according to protocols approved by the Institutional Animal Care and Use Committee (IACUC).

**Ethics approval and consent to participate** Not applicable.

**Consent for publication** Not applicable.

## References


1. Charrin S, Le Naour F, Labas V et al (2003) EWI-2 is a new component of the tetraspanin web in hepatocytes and lymphoid cells. Biochem J 373(Pt 2):409–421
2. Stipp CS, Kolesnikova TV, Hemler ME (2001) EWI-2 is a major CD9 and CD81 partner and member of a novel Ig protein subfamily. J Biol Chem 276(44):40545–40554
3. Zhang XA, Lane WS, Charrin S et al (2003) EWI2/PGRL associates with the metastasis suppressor KAI1/CD82 and inhibits the migration of prostate cancer cells. Cancer Res 63(10):2665–2674
4. Charrin S, Jouannet S, Boucheix C et al (2014) Tetraspanins at a glance. J Cell Sci 127(Pt 17):3641–3648
5. Wang H-X, Li Q, Sharma C et al (2011) Tetraspanin protein contributions to cancer. Biochem Soc Trans 39(2):547–552
6. Yáñez-Mó M, Barreiro O, Gordon-Alonso M et al (2009) Tetraspanin-enriched microdomains: a functional unit in cell plasma membranes. Trends Cell Biol 19(9):434–446
7. Yang Y-G, Sari IN, Zia MF et al (2016) Tetraspanins: spanning from solid tumors to hematologic malignancies. Exp Hematol 44(5):322–328
8. Avraham R, Yarden Y (2011) Feedback regulation of EGFR signalling: decision making by early and delayed loops. Nat Rev Mol Cell Biol 12(2):104–117
9. Berditchevski F, Odintsova E (2016) ErbB receptors and tetraspanins: casting the net wider. Int J Biochem Cell Biol 77(Pt A):68–71
10. Mitamura T, Iwamoto R, Umata T et al (1992) The 27-kD diphtheria toxin receptor-associated protein (DRAP27) from vero cells is the monkey homologue of human CD9 antigen: expression of DRAP27 elevates the number of diphtheria toxin receptors on toxin-sensitive cells. J Cell Biol 118(6):1389–1399
11. Tang M, Yin G, Wang F et al (2015) Downregulation of CD9 promotes pancreatic cancer growth and metastasis through upregulation of epidermal growth factor on the cell surface. Oncol Rep 34(1):350–358
12. Wang G-P, Han X-F (2015) CD9 modulates proliferation of human glioblastoma cells via epidermal growth factor receptor signaling. Mol Med Rep 12(1):1381–1386
13. Murayama Y, Shinomura Y, Oritani K et al (2008) The tetraspanin CD9 modulates epidermal growth factor receptor signaling in cancer cells. J Cell Physiol 216(1):135–143
14. Haeger A, Krause M, Wolf K et al (2014) Cell jamming: collective invasion of mesenchymal tumor cells imposed by tissue confinement. Biochim Biophys Acta 1840(8):2386–2395
15. Wolf K, Friedl P (2011) Extracellular matrix determinants of proteolytic and non-proteolytic cell migration. Trends Cell Biol 21(12):736–744
16. Taddei ML, Giannoni E, Comito G et al (2013) Microenvironment and tumor cell plasticity: an easy way out. Cancer Lett 341(1):80–96
17. Tester AM, Ruangpanit N, Anderson RL et al (2000) MMP-9 secretion and MMP-2 activation distinguish invasive and metastatic sublines of a mouse mammary carcinoma system showing epithelial-mesenchymal transition traits. Clin Exp Metastasis 18(7):553–560
18. Kong D, Wang Z, Sarkar SH et al (2008) Platelet-derived growth factor-D overexpression contributes to epithelial-mesenchymal transition of PC3 prostate cancer cells. Stem Cells 26(6):1425–1435
19. Sun Y, Schaar A, Sukumaran P et al (2018) TGFβ-induced epithelial-to-mesenchymal transition in prostate cancer cells is mediated via TRPM7 expression. Mol Carcinog 57(6):752–761
20. Javadi S, Zhiani M, Mousavi MA et al (2020) Crosstalk between epidermal growth factor receptors (EGFR) and integrins in resistance to EGFR tyrosine kinase inhibitors (TKIs) in solid tumors. Eur J Cell Biol 99(4):151083
21. Montanari M, Rossetti S, Cavaliere C et al (2017) Epithelial-mesenchymal transition in prostate cancer: an overview. Oncotarget 8(21):35376–35389
22. Sala-Valdés M, Ursa A, Charrin S et al (2006) EWI-2 and EWI-F link the tetraspanin web to the actin cytoskeleton through their direct association with ezrin-radixin-moesin proteins. J Biol Chem 281(28):19665–19675
23. Smith CS, Joseph N, Rieger B et al (2010) Fast, single-molecule localization that achieves theoretically minimum uncertainty. Nat Methods 7(5):373–375
24. Huang F, Schwartz SL, Byars JM et al (2011) Simultaneous multiple-emitter fitting for single molecule super-resolution imaging. Biomed Opt Express 2(5):1377–1393
25. Ester M, Kriegel H-P, Sander J et al (1996) A density-based algorithm for discovering clusters in large spatial databases with noise. In: Proceedings of the Second International Conference on Knowledge Discovery and Data Mining. Portland, OR, USA, pp 226–31
26. Daszykowski M, Walczak B, Massart DL et al (2002) Looking for natural patterns in analytical data. 2. Tracing local density with OPTICS. J Chem Inf Comput Sci 42(3):500–507
27. Johnson S, Chen H, Lo P-K (2013) In vitro tumorsphere formation assays. Bio Protoc 3(3):e325
28. Portillo-Lara R, Alvarez MM (2015) Enrichment of the cancer stem phenotype in sphere cultures of prostate cancer cell lines occurs through activation of developmental pathways mediated by the transcriptional regulator ΔNp63α. PLoS ONE 10(6):e0130118
29. He B, Zhang YH, Richardson MM et al (2011) Differential functions of phospholipid binding and palmitoylation of tumour suppressor EWI2/PGRL. Biochem J 437(3):399–411
30. Li S, Goncalves KA, Lyu B et al (2020) Chemosensitization of prostate cancer stem cells in mice by angiogenin and plexin-B2 inhibitors. Commun Biol. 3(1):26
31. Collins AT, Berry PA, Hyde C et al (2005) Prospective identification of tumorigenic prostate cancer stem cells. Cancer Res 65(23):10946–10951
32. Huang C, Fu C, Wren JD et al (2018) Tetraspanin-enriched microdomains regulate digitation junctions. Cell Mol Life Sci 75(18):3423–3439
33. Noguchi S, Saito A, Nagase T (2018) YAP/TAZ signaling as a molecular link between fibrosis and cancer. Int J Mol Sci 19(11):3674
34. Zhengming Wu, Guan K-L (2021) Hippo signaling in embryogenesis and development. Trends Biochem Sci 46(1):51–63
35. Yarden Y, Shilo B-Z (2007) SnapShot: EGFR signaling pathway. Cell 131(5):1018
36. Sigismund S, Argenzio E, Tosoni D et al (2008) Clathrin-mediated internalization is essential for sustained EGFR signaling but dispensable for degradation. Dev Cell 15(2):209–219
37. Bakker J, Spits M, Neefjes J et al (2017) The EGFR odyssey—from activation to destruction in space and time. J Cell Sci 130(24):4087–4096
38. Wang H-X, Sharma C, Knoblich K et al (2015) EWI-2 negatively regulates TGF-β signaling leading to altered melanoma growth and metastasis. Cell Res 25(3):370–385

39. Yang XH, Kovalenko OV, Kolesnikova TV et al (2006) Contrasting effects of EWI proteins, integrins, and protein palmitoylation on cell surface CD9 organization. J Biol Chem 281(18):12976–12985
40. Stipp CS (2010) Laminin-binding integrins and their tetraspanin partners as potential antimetastatic targets. Expert Rev Mol Med 12:e3
41. Gustafson-Wagner E, Stipp CS (2013) The CD9/CD81 tetraspanin complex and tetraspanin CD151 regulate α3β1 integrin-dependent tumor cell behaviors by overlapping but distinct mechanisms. PLoS ONE 8(4):e61834
42. Hong I-K, Byun H-J, Lee J et al (2014) The tetraspanin CD81 protein increases melanoma cell motility by up-regulating metalloproteinase MT1-MMP expression through the pro-oncogenic Akt-dependent Sp1 activation signaling pathways. J Biol Chem 289(22):15691–15704
43. Kotha J, Longhurst C, Appling W et al (2008) Tetraspanin CD9 regulates beta 1 integrin activation and enhances cell motility to fibronectin via a PI-3 kinase-dependent pathway. Exp Cell Res 314(8):1811–1822
44. Posor Y, Eichhorn-Grünig M, Haucke V (2015) Phosphoinositides in endocytosis. Biochim Biophys Acta 1851(6):794–804
45. Charrin S, Manié S, Thiele C et al (2003) A physical and functional link between cholesterol and tetraspanins. Eur J Immunol 33(9):2479–2489
46. Zimmerman B, Kelly B, McMillan BJ et al (2016) Cell 167(4):1041-1051.e11
47. Weber GF, Bjerke MA, DeSimone DW (2011) Integrins and cadherins join forces to form adhesive networks. J Cell Sci 124(Pt 8):1183–1193
48. Mui KL, Chen CS, Assoian RK (2016) The mechanical regulation of integrin-cadherin crosstalk organizes cells, signaling and forces. J Cell Sci 129(6):1093–1100
49. Rausch S, Das T, Soiné JRD et al (2013) Polarizing cytoskeletal tension to induce leader cell formation during collective cell migration. Biointerphases 8(1):32
50. Chenying Fu, Zhang Q, Wang A et al (2021) EWI-2 controls nucleocytoplasmic shuttling of EGFR signaling molecules and miRNA sorting in exosomes to inhibit prostate cancer cell metastasis. Mol Oncol 15(5):1543–1565
51. Hill MM, Bastiani M, Luetterforst R et al (2008) PTRF-Cavin, a conserved cytoplasmic protein required for caveola formation and function. Cell 132(1):113–124
52. Peng Wu, Wee P, Jiang J et al (2012) Differential regulation of transcription factors by location-specific EGF receptor signaling via a spatio-temporal interplay of ERK activation. PLoS ONE 7(9):e41354
53. Gayer CP, Craig DH, Flanigan TL et al (2010) ERK regulates strain-induced migration and proliferation from different subcellular locations. J Cell Biochem 109(4):711–725
54. Carraway KL 3rd, Sweeney C (2006) Co-opted integrin signaling in ErbB2-induced mammary tumor progression. Cancer Cell 10(2):93–95
55. Alexi X, Berditchevski F, Odintsova E (2011) The effect of cell-ECM adhesion on signalling via the ErbB family of growth factor receptors. Biochem Soc Trans 39(2):568–573
56. Erfani S, Hua H, Pan Y et al (2021) The context-dependent impact of integrin-associated CD151 and other tetraspanins on cancer development and progression: a class of versatile mediators of cellular function and signaling, tumorigenesis and metastasis. Cancers (Basel) 13(9):2005
57. Ramovs V, Te Molder L, Sonnenberg A (2017) The opposing roles of laminin-binding integrins in cancer. Matrix Biol 57–58:213–243